



**HAL**  
open science

## The Thermal State and Interior Structure of Mars

A.-c. Plesa, S. Padovan, N. Tosi, D. Breuer, M. Grott, M. Wiczorek, T. Spohn, S. Smrekar, W. Banerdt

► **To cite this version:**

A.-c. Plesa, S. Padovan, N. Tosi, D. Breuer, M. Grott, et al.. The Thermal State and Interior Structure of Mars. *Geophysical Research Letters*, 2018, 45 (22), pp.12,198-12,209. 10.1029/2018GL080728 . hal-02307608

**HAL Id: hal-02307608**

**<https://hal.science/hal-02307608>**

Submitted on 26 Jun 2020

**HAL** is a multi-disciplinary open access archive for the deposit and dissemination of scientific research documents, whether they are published or not. The documents may come from teaching and research institutions in France or abroad, or from public or private research centers.

L'archive ouverte pluridisciplinaire **HAL**, est destinée au dépôt et à la diffusion de documents scientifiques de niveau recherche, publiés ou non, émanant des établissements d'enseignement et de recherche français ou étrangers, des laboratoires publics ou privés.

# Geophysical Research Letters

## RESEARCH LETTER

10.1029/2018GL080728

### Key Points:

- We combine the largest-to-date set of 3-D dynamical models with observations to constrain the thermal state and interior structure of Mars
- Best-fit models suggest a core radius strictly larger than 1,800 km and an average crustal thickness  $48.8 \text{ km} < d_c < 87.1 \text{ km}$
- Models suggest a large pressure dependence of the viscosity and a crust containing 65–70% of the total amount of heat producing elements

### Supporting Information:

- Supporting Information S1
- Data Set S1
- Data Set S2

### Correspondence to:

A.-C. Plesa,  
Ana.Plesa@dlr.de

### Citation:

Plesa, A.-C., Padovan, S., Tosi, N., Breuer, D., Grott, M., Wieczorek, M. A., et al. (2018). The thermal state and interior structure of Mars. *Geophysical Research Letters*, 45, 12,198–12,209. <https://doi.org/10.1029/2018GL080728>

Received 22 AUG 2018

Accepted 5 NOV 2018

Accepted article online 9 NOV 2018

Published online 28 NOV 2018

## The Thermal State and Interior Structure of Mars

A.-C. Plesa<sup>1</sup> , S. Padovan<sup>1</sup> , N. Tosi<sup>1,2</sup> , D. Breuer<sup>1</sup> , M. Grott<sup>1</sup> , M. A. Wieczorek<sup>3</sup> , T. Spohn<sup>1</sup>, S. E. Smrekar<sup>4</sup>, and W. B. Banerdt<sup>4</sup>

<sup>1</sup>German Aerospace Center (DLR), Berlin, Germany, <sup>2</sup>Technische Universität Berlin, Berlin, Germany, <sup>3</sup>Université Côte d'Azur, Observatoire de la Côte d'Azur, CNRS, Laboratoire Lagrange, France, <sup>4</sup>Jet Propulsion Laboratory, California Institute of Technology, Pasadena, CA, USA

**Abstract** The present-day thermal state, interior structure, composition, and rheology of Mars can be constrained by comparing the results of thermal history calculations with geophysical, petrological, and geological observations. Using the largest-to-date set of 3-D thermal evolution models, we find that a limited set of models can satisfy all available constraints simultaneously. These models require a core radius strictly larger than 1,800 km, a crust with an average thickness between 48.8 and 87.1 km containing more than half of the planet's bulk abundance of heat producing elements, and a dry mantle rheology. A strong pressure dependence of the viscosity leads to the formation of prominent mantle plumes producing melt underneath Tharsis up to the present time. Heat flow and core size estimates derived from the InSight (Interior Exploration using Seismic Investigations, Geodesy and Heat Transport) mission will increase the set of constraining data and help to confine the range of admissible models.

**Plain Language Summary** We constrain the thermal state and interior structure of Mars by combining a large number of observations with thermal evolution models. Models that match the available observations require a core radius larger than half the planetary radius and a crust thicker than 48.8 km but thinner than 87.1 km on average. All best-fit models suggest that more than half of the planet's bulk abundance of heat producing elements is located in the crust. Mantle plumes may still be active today in the interior of Mars and produce partial melt underneath the Tharsis volcanic province. Our results have important implications for the thermal evolution of Mars. Future data from the InSight (Interior Exploration using Seismic Investigations, Geodesy and Heat Transport) mission can be used to validate our models and further improve our understanding of the thermal evolution of Mars.

### 1. Introduction

Tectonic and volcanic features on rocky planets like Mars are directly linked to processes in the interior that have been active for up to billions of years. A large volume of geophysical and geochemical data on the planet have become available from space missions and analyses of martian meteorites. Still, the thermal evolution of the interior is poorly known, and a number of issues are unsolved: (1) The large elastic lithosphere thickness underneath the north pole of Mars (Phillipsetal, 2008) is hard to reconcile with the well-accepted compositional model WD94 (Wänke & Dreibus, 1994), should this large elastic thickness be representative of the global average. The WD94 model is based on element correlations measured for the martian meteorites and shows Th/K ratios in close agreement with the surface abundance of heat producing elements, HPE (Taylor et al., 2006). Since the WD94 heat production rate implies a smaller average elastic lithosphere thickness than the north pole estimate, it has been argued that the bulk abundance of HPE in Mars could be lower than previously estimated by geochemical models (Phillips et al., 2008) or that the north pole elastic thickness is not representative of the entire planet (Grott & Breuer, 2010; Kiefer & Li, 2009; Phillips et al., 2008; Plesa et al., 2016). (2) The surface abundance of HPE derived from gamma-ray measurements indicate a significant enrichment of HPE in the crust, suggesting a present-day crustal heat production rate of 49 pW/kg (Hahn et al., 2011; Taylor et al., 2006). However, gamma-ray measurements can only map the uppermost 10 cm of the crust, and little is known about the HPE distribution in deeper layers. (3) Gravity and topography data have been used to derive maps of the thickness of the martian crust. The results are non-unique; inferred crustal thicknesses vary between 30 and 87 km for uniform crustal densities between 2,700 and 3,200 kg/m<sup>3</sup> (Plesa et al., 2016; Wieczorek & Zuber, 2004). In addition, the difference in crustal thickness between the northern and southern

hemispheres (the so-called crustal thickness dichotomy) can be reduced if the crustal density varied between the two hemispheres (Goossens et al., 2017; Plesa et al., 2016). (4) Large volcanic provinces such as Tharsis and Elysium have been active over most of the evolution of Mars (e.g., Hauber et al., 2011; Neukum et al., 2004; Werner, 2009) suggesting the presence of long-lived mantle plumes. Whether such mantle plumes are still active today is unknown. (5) Planet formation scenarios as well as geological and petrological evidence suggest that the martian mantle must have contained at least few tens of parts per million (ppm) water (e.g., Brasser, 2013; Dreibus & Wänke, 1985) at the end of accretion, sufficient for significant rheological weakening (Hirth & Kohlstedt, 2003; Karato & Wu, 1993). The initial mantle inventory was likely reduced by dehydration during partial melting (e.g., Morschhauser et al., 2011), but the present-day water concentration in the mantle and its rheological significance is much-debated (see Filiberto, Baratoux, et al., 2016, for a recent review). Constraints on the present-day water inventory in the interior of Mars come from the analysis of martian meteorites. Recent studies suggest a water content  $< 130$  ppm (Filiberto, Gross, et al., 2016) and even as low as  $14 - 23$  ppm from the analysis of depleted shergottites (McCubbin et al., 2016).

Parameterized as well as 2-D and 3-D convection models (Breuer & Moore, 2015) of the thermal evolution of Mars have been used to explain, for example, the formation of the crustal thickness dichotomy, the formation of a super plume underneath Tharsis (e.g., Golabek et al., 2011; Keller & Tackley, 2009; Roberts & Zhong, 2006), and the magmatic and crust formation history (e.g., Breuer & Spohn, 2006; Fraeman & Korenaga, 2010; Hauck & Phillips, 2002; Morschhauser et al., 2011; Plesa & Breuer, 2014; Ruedas et al., 2013). Other mantle convection models studied the cooling and solidification of a putative liquid magma ocean (e.g., Elkins-Tanton et al., 2005; Maurice et al., 2017; Plesa et al., 2014; Tosi, Plesa, et al., 2013) and the effects of large-scale impacts on the interior dynamics (e.g., Roberts & Arkani-Hamed, 2017; Ruedas & Breuer, 2017). In this study we compare the results of the largest set of numerical simulations to date of the thermal evolution of Mars in 3-D spherical geometry with available observations in order to identify key parameters that control the interior evolution. The calculations will provide a tool to support the overall interpretation of data from the upcoming Interior exploration using Seismic Investigations, Geodesy and Heat Transport (InSight) mission (Banerdt & Russell, 2017), which will deploy a seismometer and a heat flow probe in the Elysium Planitia region on Mars to record seismic data and measure the surface heat flow for a martian year.

## 2. Methods

We ran 130 models in 3-D spherical geometry using the mantle convection code Gaia (Hüttig & Stemmer, 2008a, 2008b; Hüttig et al., 2013). Model details are described in Plesa et al. (2015, 2016) and in supporting information S1. In our models we varied the following input parameters: initial mantle temperature, core size, mantle reference viscosity, pressure, and temperature dependence of the viscosity (Hirth & Kohlstedt, 2003; Karato & Wu, 1993), a constant or a temperature- and pressure-dependent mantle thermal expansivity (Tosi, Yuen, et al., 2013), thickness and thermal conductivity of the crust, and the amount and distribution of HPE in the interior. Most simulations employ the bulk abundance of HPE of the WD94 compositional model, but some cases assume a lower amount (see Table S1). All simulations consider a nominally anhydrous mantle. However, we test reference viscosities between  $10^{20}$  Pa s, considering the viscosity lowering due to the presence of a few tens of ppm water (Hirth & Kohlstedt, 2003; Karato & Wu, 1993), and  $10^{21}$  Pa s, corresponding to a dry mantle rheology. We use crustal thickness models derived from gravity and topography data that we keep constant in time. Crustal densities vary between  $2,700$  and  $3,200$  kg/m<sup>3</sup>, and for one model, we employ a density of  $2,900$  kg/m<sup>3</sup> for the southern highlands and  $3,100$  kg/m<sup>3</sup> for the northern lowlands using the dichotomy boundary of Andrews-Hanna et al. (2008). Further details of the crustal thickness models are discussed in Wicczorek et al. (2013) and Plesa et al. (2016). The crust is homogeneously enriched in HPE, such that we obtain a present-day heat production rate  $H_{cr} = 49$  pW/kg in agreement with gamma-ray data (see supporting information S1 for further details). As the concentration of HPE in the deep crust is poorly known, we tested the sensitivity of our results by running additional cases, for which the present-day  $H_{cr}$  lies between  $9.8$  and  $98$  pW/kg (i.e., 5 times lower and 2 times higher than the average value suggested by gamma-ray data).

All constraints considered are related to the interior temperature distribution, either directly (potential temperature inferred from shergottite mineralogy and occurrence of present-day melting) or indirectly (tidal Love number  $k_2$ , dissipation factor  $Q$ , and elastic lithosphere thickness). The tidal Love number  $k_2$  provides a strong constraint on the interior structure of the planet, given its sensitivity to the size of the liquid core (Rivoldini et al., 2011; Van Hoolst et al., 2003; Yoder et al., 2003). A detailed description of the constraints used is given in supporting information S1.

We compute  $k_2$  at the period of the semidiurnal Solar tide for the entire set of convection models (Moore & Schubert, 2000; Padovan et al., 2014) and find only the subset of models with a radius of 1,850 km to be compatible with the most recent estimate for this observable,  $k_2 = 0.169 \pm 0.006$  (Konopliv et al., 2016). In computing  $k_2$ , we use the Andrade pseudoperiod model (Jackson et al., 2010; Padovan et al., 2014), which accounts for the nonelastic response of mantle rock at tidal frequencies, to obtain a rheological profile (see model description in supporting information S1). Thus, as part of the calculation, we estimate the tidal quality factor  $Q$  at the semidiurnal tide of Phobos. Our result is in line with previous work: Yoder et al. (2003) provide a range of core radii between 1,520 and 1,840 km for  $k_2$  ranging between 0.136 and 0.170; Rivoldini et al. (2011) find the core radius between 1,800 and 1,900 km for a  $k_2$  of 0.17. A recent study (Khan et al., 2017) that applied an inversion technique similar to the one used in Rivoldini et al. (2011), obtained slightly smaller core radii between 1,730 and 1,840 km when using the latest  $k_2$  estimate (Genova et al., 2016; Konopliv et al., 2016). The small discrepancy between their and our result is likely due to differences in the viscoelastic model employed (Khan et al., 2017).

$Q$  is mostly sensitive to the viscosity profile (Nimmo & Faul, 2013), which in turn depends strongly on the mantle temperature, the grain size, and possibly the iron content (Zhao et al., 2009). While a number of parameters enter the calculation of  $Q$  and some of them are not well known for Mars (see additional discussion in supporting information S1), for a given core radius the hotter the mantle, the lower is  $Q$  (i.e., the more dissipative is the mantle). By computing  $Q$  for each convection model—allowing for variations of unknown parameters (e.g., activation energy)—and comparing the results with the range  $99.5 \pm 4.9$  inferred from the orbital acceleration of Phobos (Konopliv et al., 2011; Lainey, 2016), we find that models with inefficient heat transport remain too hot (i.e., too dissipative) to satisfy the tidal quality factor constraint. This may be caused by a too large pressure dependence of the viscosity (e.g., an activation volume of  $20 \text{ cm}^3/\text{mol}$ ) or by a too large concentration of HPE in the mantle. The latter may be caused by either a low crustal enrichment (e.g., present-day  $H_{cr}$  of only  $9.8 \text{ pW/kg}$ ) or, alternatively, by a crust thinner than 45 km with present-day  $H_{cr} = 49 \text{ pW/kg}$  as suggested by the gamma-ray data. Conversely, the mantle is too cold and not dissipative enough if the HPE concentration in the mantle is too small. The latter is observed for models with  $H_{cr} = 49 \text{ pW/kg}$  at present day and an average crustal thickness  $\geq 87 \text{ km}$ .

By calculating the mechanical lithosphere thickness, we obtain an upper bound for the elastic lithosphere thickness (see supporting information S1 for mechanical lithosphere thickness calculations), which we compare with available estimates for the Noachian epoch and for the present-day north and south polar regions. The mechanical lithosphere thickness can be mapped by tracing the isotherm that is associated with the onset of ductile deformation (Burov & Diament, 1995). That thickness is similar to the effective elastic thickness if the lithospheric plate has a small curvature and bending moment (McNutt, 1984). A small elastic lithosphere thickness for the Noachian suggests a thin thermal boundary layer, vigorous mantle convection, and/or a warm lithosphere (Grott et al., 2013). A warm lithosphere can be obtained if the bulk of the crust has already been emplaced during the Noachian and contains  $>40\%$  of the total HPE inventory of the WD94 compositional model. Present-day localized melting, the high potential temperatures inferred from the mineralogy of the shergottites (Filiberto & Dasgupta, 2015), and a present-day elastic lithosphere thickness of at least 110 km at the south pole of Mars (Wieczorek, 2008) require a mantle moderately depleted in HPE and a crust thinner than 87 km on average. Models with an average crustal thickness of 87 km and present-day  $H_{cr} = 49 \text{ pW/kg}$  have a strongly depleted mantle that cools too rapidly and does not produce melt late in the thermal evolution, not even locally. At the same time, the elastic thickness values are smaller than the available present-day south pole estimate, due to the insulating effect of the thick southern crust. Decreasing the crustal heat production rate would lead to smaller lithospheric temperatures and consequently to a thicker present-day elastic lithosphere at the south pole but would suggest an elastic lithosphere in the Noachian thicker than estimated.

### 3. Results

The results of our 130 thermal evolution calculations are summarized in Figure 1, and the nine best-fit models (cases 51, 84, 85, 94, 97, 117, 118, 121, and 129 in Table S2) are identified. All best-fit models share a dry mantle rheology with a reference viscosity of  $10^{21} \text{ Pa s}$  and a wet crustal rheology. The latter is required to obtain small elastic lithosphere thickness values for the Noachian epoch. Some successful models have a large activation volume of  $10 \text{ cm}^3/\text{mol}$  implying a strong pressure dependence of the viscosity. Others (cases 117 and 118) have a moderate value of  $6 \text{ cm}^3/\text{mol}$  but adopt a proposed 50-fold viscosity increase in the mid-mantle, possibly caused by a mineralogical transition zone (Keller & Tackley, 2009). All successful models are

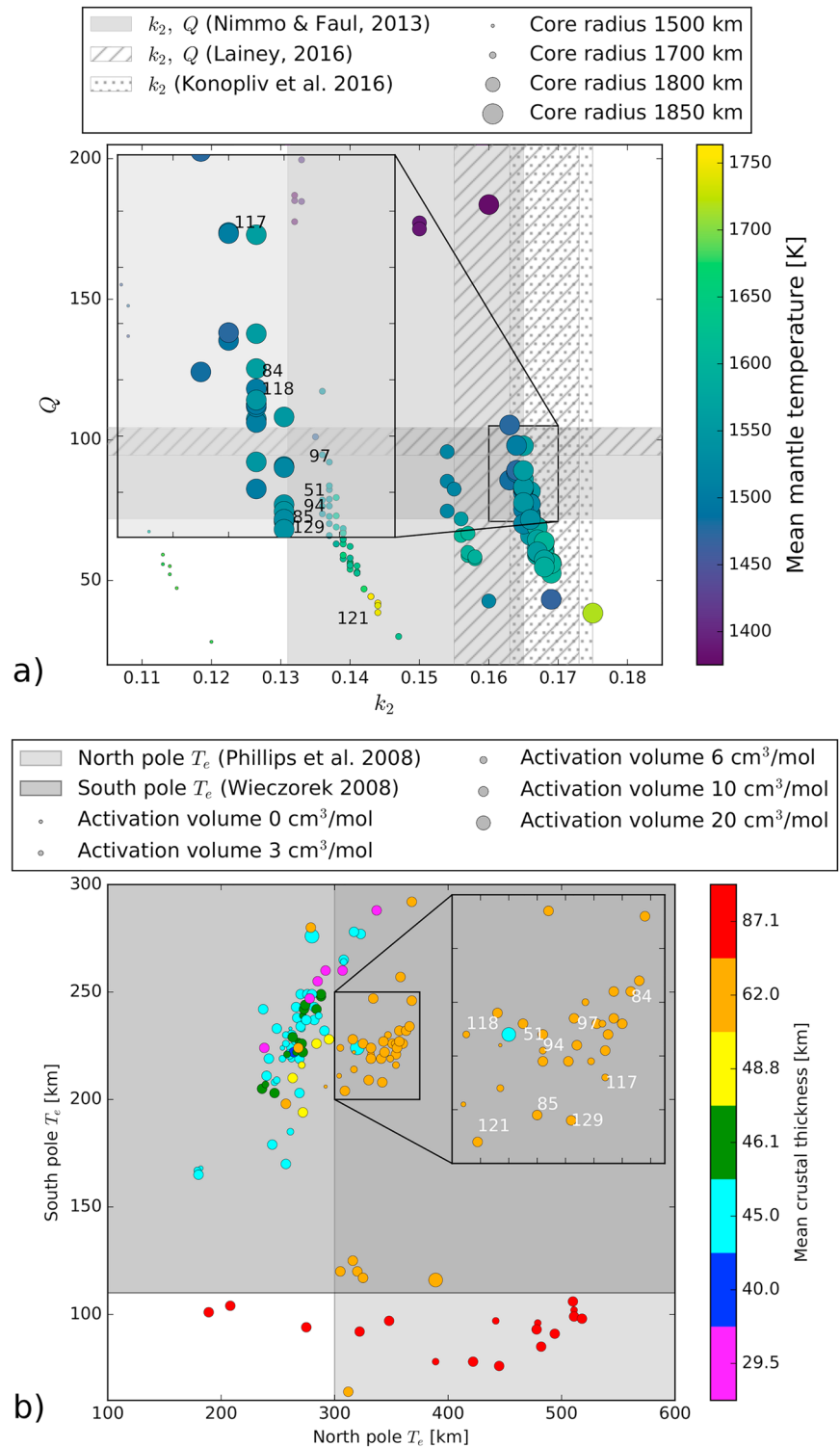


**Figure 1.** Results of the model calculations comparing tidal parameter and present-day elastic lithosphere thickness constraints. (a)  $k_2$  and  $Q$ . Each symbol represents one model. The size of the symbols is proportional to the size of the core as given in the legend. Colors indicate the mean mantle temperature. (b) Present-day elastic lithosphere thickness values underneath the polar caps which extend to  $5^\circ$  from the south and  $10^\circ$  from the north pole. The size of the symbols shows the activation volume and hence indicates the strength of the pressure dependence of the viscosity. Colors show the average crustal thickness used in the simulations. Best-fit models are indicated by their case number (See Table S1 for the parameters of these models). The gray and hatched areas on both panels show available estimates for  $k_2$ ,  $Q$ , and the elastic lithosphere thicknesses at the north and south poles of Mars. Note that the areas of successful models have been enlarged for clarity in both panels.

characterized by inefficient heat transport from the deep mantle caused by the large viscosity there. The viscosity of the lower mantle is 9 to 721 times higher than that of the upper mantle in these models. Average temperature profiles are similar for cases using a small and a large activation volumes (i.e., 0 and 10 cm<sup>3</sup>/mol), but the temperature variations are larger by more than 160 K for the case using a large pressure dependence of the viscosity (Figure S4). As the mantle cools and the thermal lithosphere on top of the convecting mantle thickens, the viscosity contrast across the convecting mantle decreases in time (Figure S5).

The average crustal thickness of all best-fit models is 62 km, in agreement with the upper range of values found by Wieczorek and Zuber (2004), and the crust is strongly enriched in HPE, with a present-day  $H_{cr}$  of 44.1–49 pW/kg. Cases with a thinner crust require  $H_{cr}$  at least 1.2 and 1.7 times higher than the gamma-ray measurements for crustal thicknesses of 45 and 29.5 km, respectively, to satisfy the large present-day elastic lithosphere thickness at the north pole (cases 109 and 126). However, a large enrichment of the crust makes it difficult to obtain present-day melting in the mantle, even when using the most recent solidus estimates of the martian mantle (Kiefer et al., 2015; Ruedas & Breuer, 2017), as the latter is considerably depleted. In addition, a thin crust is less efficient in insulating the mantle. Crustal heat production rates higher than the ones suggested by the gamma-ray data cannot be excluded on a local scale. However, they are not likely to be globally representative as this would result in large-scale remelting of the basaltic crust. Since there is no evidence for widespread tertiary crust in the gamma-ray data (Taylor et al., 2006), we consider models employing a crustal enrichment in HPE larger than the value suggested by gamma-ray measurements only marginally relevant.

All best-fit models have a large core with a radius of 1,850 km for consistency with the latest  $k_2$  estimate of  $0.169 \pm 0.006$  (Konopliv et al., 2016). A core radius of 1,850 km also helps to explain the presently thick elastic lithosphere underneath the north pole as a thinner mantle contains smaller amounts of HPE when compared to models with a smaller core. However, the high potential temperatures required by the shergottite mineralogy are more difficult to explain for large core models. For a core radius of 1,500 km, high mantle temperatures are easily obtained, but the present-day elastic thicknesses at the north and south poles of Mars cannot be matched. If we consider smaller  $k_2$  values of 0.136, this would allow models with a smaller core radius (models 41, 42, and 130 have core radii of 1,700 and 1,800 km). Other parameters of these models are similar to those of the nine best-fit models.

The present-day elastic lithosphere thicknesses at the north and south poles of Mars constitute a particularly tight constraint. If we relaxed the limit of  $\geq 300$  km for the north polar elastic lithosphere thickness by 20 km and that for the south pole of  $\geq 110$  km by 10 km, three additional models would satisfy the requirements (cases 88, 110, and 120 in Table S1). While the rheological parameters remain unchanged from the nine best-fit cases, models with an average crustal thickness of 45 km (cases 110 and 120) and 46 km (case 88) become acceptable. In addition, if both the present-day elastic thicknesses and the  $k_2$  estimate are relaxed, another case employing a crustal thickness of 48.8 km becomes compatible with observations (case 36). Still, the crustal HPE content needs to be high, requiring a present-day  $H_{cr}$  to be 49–59 pW/kg.

The most relevant parameters of the best-fit models are listed in Table 1, while lists of all parameters and results for each individual model are included in supporting information S1.

In the following, we discuss a model representative of the nine best-fit models in more detail (Figure 2). Although we will be referring to this model as the *reference model*, we emphasize that it is by no means better than the other eight models. The reference model (case 85) differs from other best-fit models by having a high initial mantle temperature of 1,850 K compared to 1,650 K used in cases 84, 117, and 129, a slightly higher activation energy of 325 kJ/mol compared to 300 kJ/mol used in case 51. Cases 117 and 118 employ a smaller activation volume of only 6 cm<sup>3</sup>/mol but use an additional 50-fold viscosity increase in the midmantle. In the reference case we use the WD94 compositional model, but other best-fit models use a smaller amount of HPE than WD94 by assuming a lower concentration by up to 10% in the crust (case 94) or in the mantle (case 97). The effects of varying the HPE abundances are discussed in supporting information S1.

We note that all nine best-fit models show present-day mantle plumes underneath Tharsis and Elysium, with the Tharsis plume still producing partial melt today. The location of mantle plumes is affected by the crustal thickness distribution and crustal content of HPE. Mantle plumes either originate or migrate during the first billion year of evolution beneath regions covered by a thick insulating crust. This has been observed also in previous studies that have investigated the thermal insulation of a thick crust (Schumacher & Breuer, 2006)

**Table 1**  
Mantle Parameters of the Best-Fit Models

Parameter	Value	Unit
Core radius <sup>a</sup>	>1,800	km
Average crustal thickness <sup>b</sup>	$48.8 < d_c < 87.1$	km
Initial bulk abundance of HPE	21.3–23	pW/kg
Present-day bulk abundance of HPE	3.8–4.1	pW/kg
Initial crustal heat production rate	247.5–275	pW/kg
Present-day crustal heat production rate	44.1–49	pW/kg
Mantle reference viscosity	$10^{21}$	Pa s
Activation volume	10 or 6 with additional 50-fold viscosity increase	cm <sup>3</sup> /mol
Present-day mantle HPE (of the present-day bulk HPE inventory) <sup>c</sup>	30–34.6%	—

*Note.* The values are compatible with all observational constraints used in this study. See supporting information S1 for additional parameters used in each individual thermal evolution model. HPE = heat producing elements.

<sup>a</sup>All best-fit models use a core radius of 1,850 km. While slightly smaller or larger core radii may fit the  $k_2$  estimate, no model with a core radius of 1,800 km has been found admissible. <sup>b</sup>All best-fit models use an average crustal thickness of 62 km. Although a slightly thinner or thicker crust might fit the observations, no models using an average crustal thickness of 48.8 km or thinner and no cases using an average crustal thickness of 87.1 km have been found compatible with our constraints. <sup>c</sup>Computed as  $100 \cdot (H_m \cdot M_m) / (H_{\text{bulk}} \cdot M_{\text{silicate}})$ , where  $H_m$  and  $H_{\text{bulk}}$  are the heat production rate in the mantle and the bulk inventory of HPE, respectively, while  $M_m$  and  $M_{\text{silicate}}$  are the mass of the mantle and the total silicate mass, respectively.

or modeled the migration of the Tharsis plume caused by differential rotation of the lithosphere (Šrámek & Zhong, 2012; Zhong, 2009). Plume migration could have been also caused by a large-scale impact onto the northern hemisphere, whose ejecta distribution led to a thick insulating southern hemisphere (Citron et al., 2018). Furthermore, a Tharsis plume track has been inferred from geologic units and crustal magnetic anomalies in the southern hemisphere (Hynek et al., 2011) and has been found consistent with a path of thick crust, which was identified in crustal thickness models accounting for rotational effects on shape and geoid (Cheung & King, 2014).

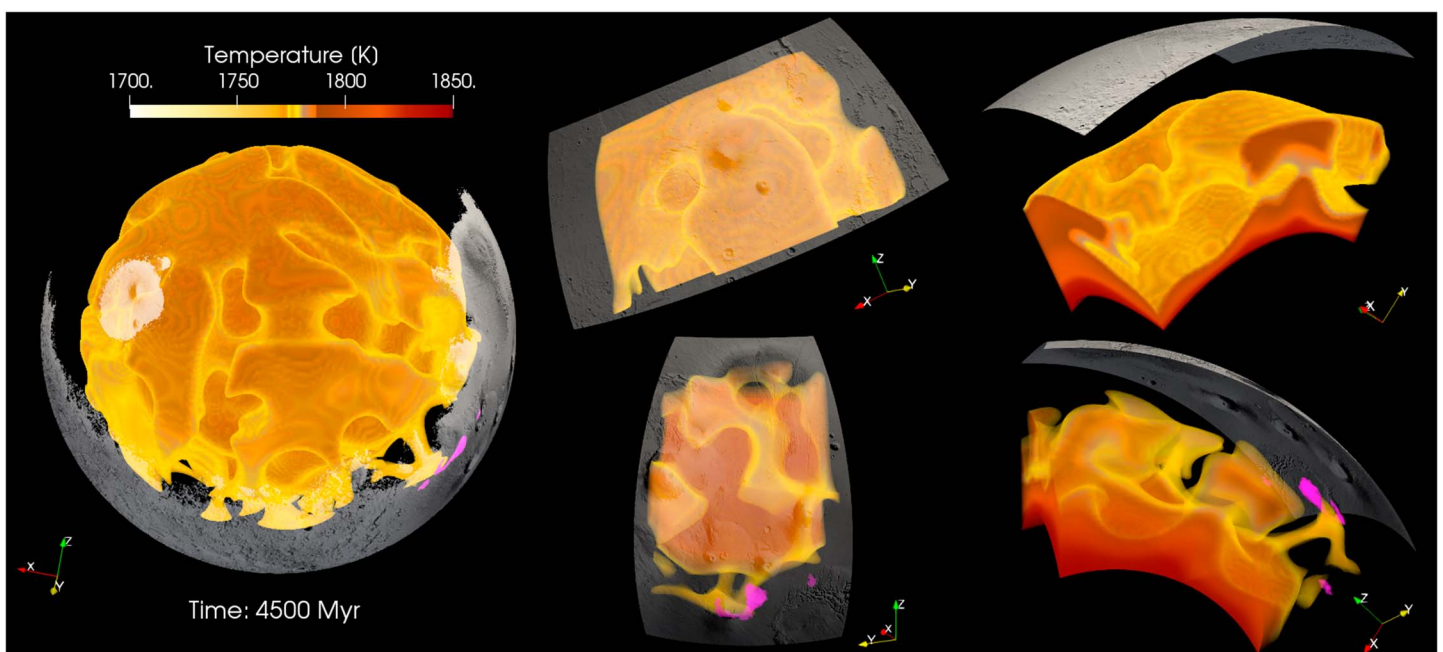


**Figure 2.** Present-day convection pattern. Mantle plumes of the reference model (case 85 in supporting information S1) are located underneath the large volcanic centers Tharsis (top row right) and Elysius (bottom row right). Although there are mantle plumes in addition to the ones underneath Tharsis and Elysius, we note that the Tharsis plume is stable through most of the thermal evolution and produces partial melt up to the present day (shown in pink color). The surface of Mars is based on a Mars Orbiter Laser Altimeter shaded relief map, which was converted to gray scale colors and shows only regions covered by a thick crust.

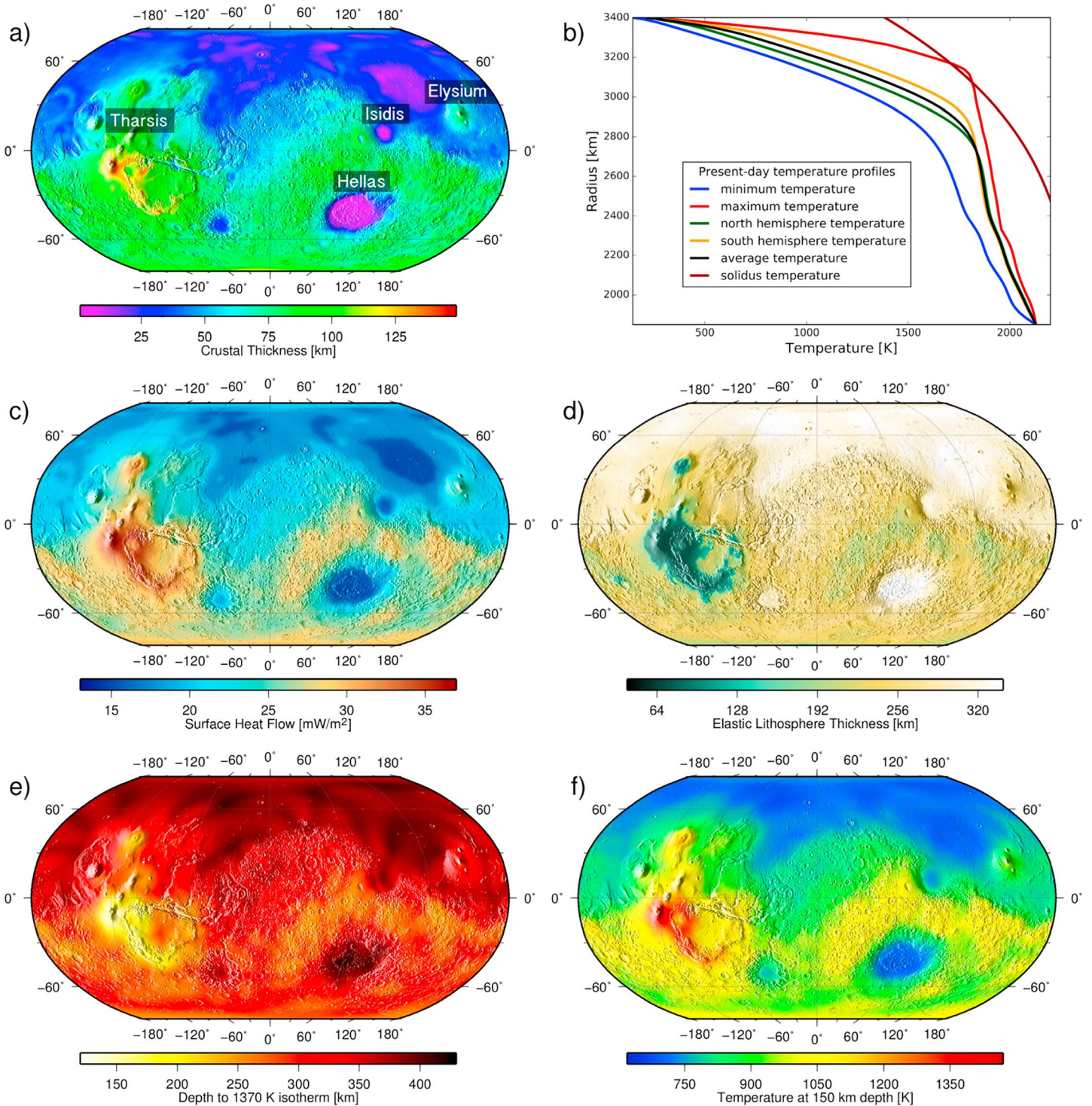


**Figure 3.** Crustal thickness distribution (a) and temperature profiles through the mantle (b) as well as maps of the surface heat flow (c), elastic lithosphere thickness (d), depth to the 1,370-K isotherm (e), and temperature at 150-km depth (f) for the reference model at present day. The model assumes a lower thermal conductivity of the crust compared to the mantle ( $3$  vs.  $4 \text{ W} \cdot \text{m}^{-1} \cdot \text{K}^{-1}$ ). The elastic thickness has been computed using the deformation time scale given by the polar cap deposition to have a better comparison with the present-day elastic thickness at the north pole. The temperature profile underneath the northern hemisphere has been computed for regions covered by a crust smaller than the average crustal thickness while for the southern hemisphere for regions covered by a crust larger than or equal to the average value.

The long-wavelength topographic and geoid anomalies at degree 2 and 3 associated with the Tharsis province are best explained by volcanic loading and downward displacement of the lithosphere rather than in terms of dynamic uplift by a mantle plume (Zhong & Roberts, 2003), an inference that is also consistent with the observed fault patterns around the region (Banerdt et al., 1992). The plume beneath Tharsis in our reference model agrees with this scenario. Although it generates a substantial dynamic geoid, it contributes to the power spectrum only at degrees between about 4 and 8.

Figures 3a and 3b show the crustal thickness model, which was employed in this specific case, and temperature profiles throughout the mantle at present day, respectively. The largest temperature differences are found in the uppermost 500 km and are caused by the combined effect of crustal thickness variations, HPE content of the crust, and the underlying convection pattern. We observe a clear dichotomy in temperature for the uppermost 600 km (green and orange lines in Figure 3b), reflecting the difference between the thick insulating crust in the southern hemisphere and the thin crust in the northern hemisphere, which allows for a stronger cooling of the underlying northern hemisphere mantle. In fact, such a temperature distribution pattern is found for all best fit-models, with peak-to-peak variations of 753–891 K at depths of 211–260 km. The large temperature variations predicted from our models may imply a seismic wave velocity dichotomy in the mantle and should be considered for the interpretation of InSight seismic data.

The variations of the present-day surface heat flow, elastic lithosphere thickness, of the depth to the 1,370-K isotherm marking the bottom of the stagnant-lid, and of temperature distribution at 150-km depth (Figures 3c–3f, respectively) closely mirror the crustal thickness variations showing a small heat flow and large elastic thickness in regions overlain by a thin crust (e.g., Hellas and Isidis impact basins). Large heat flow and small elastic thickness values are observed for the Tharsis province where the crust is thick. Some local areas, in particular in the southern hemisphere around Hellas and in and around the Tharsis region, show the presence of mantle plumes through a relatively high heat flow (Figure 3c), a thin elastic thickness (Figure 3d), shallow depth to the 1,370-K isotherm (Figure 3e), and a relatively high temperature compared to surrounding regions (Figure 3f). These mantle plumes might have once fed volcanoes like Tyrrhena and Malea Patera of the Circum-Hellas volcanic province or Nili and Meroe Patera of the Syrtis Major province.

#### 4. Discussion

Earlier studies using parameterized convection models required a rheologically significant amount of water in the martian mantle to explain the thin elastic lithosphere inferred for the Noachian (Grott & Breuer, 2008, 2009). These studies assumed a uniform crustal thickness, while ours includes a suite of spatially varying crustal thickness models based on geophysical data. We find the interior of Mars to have a high reference viscosity representative of a dry mantle rheology, in agreement with other recent petrological and geodynamical studies (Breuer et al., 2016; Filiberto, Gross, et al., 2016; McCubbin et al., 2016; Thiriet et al., 2018). The thick crust covering the southern hemisphere together with a significant enrichment in HPE as suggested by gamma-ray spectroscopy data allows a thin elastic lithosphere during the Noachian even for a dry mantle. In fact, if the interior of the planet had contained significant amounts of water, our results require that much of the water must have been lost to the atmosphere and/or stored in the crust early on, for example, through crust formation. A wet mantle rheology during most of the evolution would have resulted in significant cooling of the interior and weaker present-day mantle plumes, which cannot be reconciled with evidence for recent local high mantle temperatures (Filiberto, 2017; Filiberto & Dasgupta, 2015; Kiefer & Li, 2016; Musselwhite et al., 2006). This conclusion strengthens similar conclusions from previous 1-D models (Morschhauser et al., 2011).

Our results suggest that the martian mantle viscosity strongly increases with pressure and indicate an activation volume  $V = 10 \text{ cm}^3/\text{mol}$ . This value is higher than values used in previous geodynamical models (e.g., Keller & Tackley, 2009; Kiefer & Li, 2016; Plesa & Breuer, 2014; Ruedas et al., 2013; Šrámek & Zhong, 2012) but agrees with recent rheological studies for Mars and the upper mantle of the Earth (Dixon & Durham, 2018; Raterron et al., 2017). The large pressure dependence can explain the formation and stability of prominent mantle plumes implying spatial temperature variations in the deep mantle. At shallower depths ( $\leq 600 \text{ km}$ ), however, temperature is mostly controlled by the crustal thickness pattern with mantle plumes imprinting smaller additional variations.

Our models require that the bulk of the crust was formed early in the history of Mars such that the thick insulating crust over the southern hemisphere leads to small elastic lithosphere thicknesses during the Noachian epoch. Indeed, geological evidence suggests that the bulk of the crust has been built early during

the planetary evolution (Greeley & Schneid, 1991; Nimmo & Tanaka, 2005). All our best-fit models use a 62-km-thick crust with a uniform density of  $3,100 \text{ kg/m}^3$ , in excellent agreement with petrological analyses of martian meteorites and surface rocks (Baratoux et al., 2014). A present-day crustal heat production rate of  $44.1\text{--}49 \text{ pW/kg}$  is in good agreement with the gamma-ray measurements (Hahn et al., 2011) and with a recent study (Thiriet et al., 2018), which employed parameterized thermal evolution models to investigate the thickness and enrichment of the southern and northern martian crusts. The present-day mantle would then contain only about 30–35% of the current bulk HPE inventory. Models employing a crust of 45 km or thinner require a higher crustal heat production rate to match the present-day thick elastic lithosphere at the north pole and at the same time have difficulties to explain recent melt production in the interior.

The lower amount of Th and K obtained by the analyses of martian meteorites led to the conclusion that crustal HPE content might decrease with depth (Newsom et al., 2007). However, models with a mantle HPE content higher than 52% of the bulk WD94 compositional model cannot obtain a large present-day elastic thickness at the north pole of Mars. Although the analyses of martian meteorites and surface rocks at Gale crater seem to indicate larger differences in the crustal HPE content (Sautter et al., 2016), the gamma-ray data show little spatial variation in the surface abundance of HPE (Hahn et al., 2011). This suggests that the variations indicated by meteorites and surface rocks samples are on spatial scales below the resolution of our models and do not affect our conclusions.

The most recent  $k_2$  estimates can be matched if the core radius is  $\geq 1,850 \text{ km}$ . While slightly smaller or larger core radii may fit the latest  $k_2$  estimates, our models require that the core radius is strictly larger than 1,800 km. Thus, our models confirm previous studies of the interior structure of Mars (Rivoldini et al., 2011). A large core would contain a significant amount of light constituent to match mass and moment of inertia constraints. If sulfur were the only light element, about 17 wt% (Rivoldini et al., 2011) would be required. This much sulfur places the core close to the eutectic composition and suggests a melting temperature smaller than 1,600 K. Thus, the core would most likely be entirely liquid today as has been suggested by Schubert and Spohn (1990).

## 5. Conclusions

We have employed the largest-to-date set of numerical simulation of thermal evolution in a 3-D geometry and used a considerable number of observational data to constrain the thermal state and interior structure of Mars. Our models suggest a core radius strictly larger than 1,800 km and an average crustal thickness larger than 48.8 km but lower than 87.1 km, with an average crustal density between  $3,000$  and  $3,200 \text{ kg/m}^3$ . In addition, a large amount of HPE in the crust (i.e., 65.4–70 % of the bulk HPE inventory) and a large pressure dependence of the viscosity (i.e., an activation volume  $V = 10 \text{ cm}^3/\text{mol}$ ) are required to match the observations. A smaller core and a thinner crust or a crust more enriched in HPE could match the observations provided that the  $k_2$  and the north and south pole present-day elastic thickness constraints are relaxed. However, the rheological parameters (i.e., a large pressure dependence of the viscosity and a dry mantle rheology) would not be affected, suggesting that the martian mantle viscosity is robustly constrained. Future data on the crustal thickness and core size as well as direct estimates of the surface heat flow from the InSight mission can be used to validate our findings and further improve our models.

## References

- Andrews-Hanna, J. C., Zuber, M. T., & Banerdt, W. B. (2008). The Borealis basin and the origin of the martian crustal dichotomy. *Nature*, *453*, 1212–1215. <https://doi.org/10.1038/nature07011>
- Banerdt, W. B., Golombek, M. P., & Tanaka, K. L. (1992). Stress and tectonics on Mars. In M. George (Ed.), *Mars* (pp. 249–297). Pasadena, CA: JPL.
- Banerdt, W. B., & Russell, C. T. (2017). Editorial on: Topical collection on InSight mission to Mars. *Space Science Reviews*, *211*(1), 1–3. <https://doi.org/10.1007/s11214-017-0414-0>
- Baratoux, D., Samuel, H., Michaut, C., Toplis, M. J., Monnereau, M., Wieczorek, M., et al. (2014). Petrological constraints on the density of the martian crust. *Journal of Geophysical Research: Planets*, *119*, 1707–1727. <https://doi.org/10.1002/2014JE004642>
- Brasser, R. (2013). The formation of Mars: Building blocks and accretion time scale. *Space Science Reviews*, *174*(1), 11–25. <https://doi.org/10.1007/s11214-012-9904-2>
- Breuer, D., & Moore, W. B. (2015). Dynamics and thermal history of the terrestrial planets, the moon, and Io. *Treatise on Geophysics*, *10*(Second Ed.), 299–348. <https://doi.org/10.1016/B978-0-444-53802-4.00173-1>
- Breuer, D., Plesa, A.-C., Tosi, N., & Grott, M. (2016). Water in the martian interior—The geodynamical perspective. *Meteoritic and Planetary Science*, *51*(11), 1959–1992. <https://doi.org/10.1111/maps.12727>
- Breuer, D., & Spohn, T. (2006). Viscosity of the martian mantle and its initial temperature: Constraints from crustal formation history and the evolution of the magnetic field. *Planetary and Space Science*, *54*, 153–169. <https://doi.org/10.1016/j.pss.2005.08.008>
- Burov, E.-B., & Diament, M. (1995). The effective elastic thickness ( $T_e$ ) of continental lithosphere: What does it really mean? *Journal of Geophysical Research*, *100*, 3905–3927.

### Acknowledgments

We thank Walter S. Kiefer and an anonymous reviewer for their thoughtful comments, which helped to improve a previous version of this manuscript. All the parameters used in the models and their outcomes are listed in the online supporting information. S. P. acknowledges support by the DFG within the Research Unit FOR 2440 “Matter Under Planetary Interior Conditions”. N. T. acknowledges support from the Helmholtz Gemeinschaft (project VH-NG-1017). S. E. Smrekar and W. B. Banerdt were supported by the InSight Project, Jet Propulsion Laboratory, California Institute of Technology, under a contract with the National Aeronautics and Space Administration. Computational time has been provided by the HLRN (project bep00064), which is gratefully acknowledged. This is InSight Publication No. 65.

- Cheung, K. K., & King, S. D. (2014). Geophysical evidence supports migration of Tharsis volcanism on Mars. *Journal of Geophysical Research: Planets*, 119, 1078–1085. <https://doi.org/10.1002/2014JE004632>
- Citron, R. I., Manga, M., & Tan, E. (2018). A hybrid origin of the martian crustal dichotomy: Degree-1 convection antipodal to a giant impact. *Earth and Planetary Science Letters*, 491, 58–66. <https://doi.org/10.1016/j.epsl.2018.03.031>
- Dixon, N. A., & Durham, W. B. (2018). Measurement of activation volume for creep of dry olivine at upper-mantle conditions. *Journal of Geophysical Research: Solid Earth*, 123. <https://doi.org/10.1029/2018JB015853>
- Dreibus, G., & Wänke, H. (1985). Mars, a volatile-rich planet. *Meteoritics*, 20, 367–382.
- Elkins-Tanton, L. T., Zaranek, S. E., Parmentier, E. M., & Hess, P. C. (2005). Early magnetic field and magmatic activity on Mars from magma ocean cumulate overturn. *Earth and Planetary Science Letters*, 236, 1–12.
- Filiberto, J. (2017). Geochemistry of martian basalts with constraints on magma genesis. *Chemical Geology*, 466, 1–14.
- Filiberto, J., Baratoux, D., Beaty, D., Breuer, D., Farcy, B. J., Grott, M., et al. (2016). A review of volatiles in the martian interior. *Meteoritics & Planetary Science*, 51(11), 1935–1958.
- Filiberto, J., & Dasgupta, R. (2015). Constraints on the depth and thermal vigor of melting in the martian mantle. *Journal of Geophysical Research: Planets*, 120, 109–122. <https://doi.org/10.1002/2014JE004745>
- Filiberto, J., Gross, J., & McCubbin, F. M. (2016). Constraints on the water, chlorine, and fluorine content of the martian mantle. *Meteoritics & Planetary Science*, 51(11), 2023–2035.
- Fraeman, A. A., & Korenaga, J. (2010). The influence of mantle melting on the evolution of Mars. *Icarus*, 210(1), 43–57. <https://doi.org/10.1016/j.icarus.2010.06.030>
- Genova, A., Goossens, S., Lemoine, F. G., Mazarico, E., Neumann, G. A., Smith, D. E., & Zuber, M. T. (2016). Seasonal and static gravity field of Mars from MGS, Mars Odyssey and MRO radio science. *Icarus*, 272(Supplement C), 228–245. <https://doi.org/10.1016/j.icarus.2016.02.050>
- Golabek, G., Keller, T., Gerya, T. V., Zhu, G., Tackley, P. J., & Connolly, J. A. D. (2011). Origin of the martian dichotomy and Tharsis from a giant impact causing massive magmatism. *Icarus*, 215, 346–357. <https://doi.org/10.1016/j.icarus.2011.06.012>
- Goossens, S., Sabaka, T. J., Genova, A., Mazarico, E., Nicholas, J. B., & Neumann, G. A. (2017). Evidence for a low bulk crustal density for Mars from gravity and topography. *Geophysical Research Letters*, 44, 7686–7694. <https://doi.org/10.1002/2017GL074172>
- Greeley, R., & Schneid, B. D. (1991). Magma generation on Mars: Amounts, rates, and comparisons with Earth, moon, and Venus. *Science*, 254(5034), 996–998. <https://doi.org/10.1126/science.254.5034.996>
- Grott, M., Baratoux, D., Hauber, E., Sautter, V., Mustard, J., Gasnault, O., et al. (2013). Long-term evolution of the martian crust-mantle system. *Space Science Review*, 172(1), 49–111. <https://doi.org/10.1007/s11214-012-9948-3>
- Grott, M., & Breuer, D. (2008). The evolution of the martian elastic lithosphere and implications for crustal and mantle rheology. *Icarus*, 193, 503–515. <https://doi.org/10.1016/j.icarus.2007.08.015>
- Grott, M., & Breuer, D. (2009). Implications of large elastic thicknesses for the composition and current thermal state of Mars. *Icarus*, 201, 540–548. <https://doi.org/10.1016/j.icarus.2009.01.020>
- Grott, M., & Breuer, D. (2010). On the spatial variability of the martian elastic lithosphere thickness: Evidence for mantle plumes? *Journal of Geophysical Research*, 115, E03005. <https://doi.org/10.1029/2009JE003456>
- Hahn, B. C., McLennan, S. M., & Klein, E. C. (2011). Martian surface heat production and crustal heat flow from Mars Odyssey gamma-ray spectrometry. *Geophysical Research Letters*, 38, L14203. <https://doi.org/10.1029/2011GL047435>
- Hauber, E., Brož, P., Jagert, F., Jodłowski, P., & Platz, T. (2011). Very recent and wide-spread basaltic volcanism on Mars. *Geophysical Research Letters*, 38, L10201. <https://doi.org/10.1029/2011GL047310>
- Hauck, S. A., & Phillips, R. P. (2002). Thermal and crustal evolution of Mars. *Journal of Geophysical Research*, 107(E7), 5052. <https://doi.org/10.1029/2001JE001801>
- Hirth, G., & Kohlstedt, D. (2003). *Rheology of the upper mantle and the mantle wedge: A view from the experimentalists* (pp. 83–105). Washington, DC: American Geophysical Union. <https://doi.org/10.1029/138GM06>
- Hüttig, C., & Stemmer, K. (2008a). Finite volume discretization for dynamic viscosities on Voronoi grids. *Physics of the Earth and Planetary Interiors*, 171(1–4), 137–146. <https://doi.org/10.1016/j.pepi.2008.07.007>
- Hüttig, C., & Stemmer, K. (2008b). The spiral grid: A new approach to discretize the sphere and its application to mantle convection. *Geochemistry, Geophysics, Geosystems*, 9, Q02018. <https://doi.org/10.1029/2007GC001581>
- Hüttig, C., Tosi, N., & Moore, W. B. (2013). An improved formulation of the incompressible Navier-Stokes equations with variable viscosity. *Physics of the Earth and Planetary Interiors*, 40, 113–129.
- Hynek, B. M., Robbins, S. J., Šrámek, O., & Zhong, S. J. (2011). Geological evidence for a migrating Tharsis plume on early Mars. *Earth and Planetary Science Letters*, 310(3–4), 327–333.
- Jackson, I., Faul, U. H., Suetsugu, D., Bina, C., Inoue, T., & Jellinek, M. (2010). Grainsize-sensitive viscoelastic relaxation in olivine: Towards a robust laboratory-based model for seismological application. *Physics of the Earth and Planetary Interiors*, 183, 151–163. <https://doi.org/10.1016/j.pepi.2010.09.005>
- Karato, S. I., & Wu, P. (1993). Rheology of the upper mantle: A synthesis. *Science*, 260, 771–778.
- Keller, T., & Tackley, P. J. (2009). Towards self-consistent modeling of the martian dichotomy: The influence of one-ridge convection on crustal thickness distribution. *Icarus*, 202, 429–443.
- Khan, A., Liebske, C., Rozel, A., Rivoldini, A., Nimmo, F., Connolly, J. A. D., et al. (2017). A geophysical perspective on the bulk composition of Mars. *Journal of Geophysical Research: Planets*, 123, 575–611. <https://doi.org/10.1002/2017JE005371>
- Kiefer, W. S., Filiberto, J., Sandu, C., & Li, Q. (2015). The effects of mantle composition on the peridotite solidus: Implications for the magmatic history of Mars. *Geochimica et Cosmochimica Acta*, 162, 247–258.
- Kiefer, W. S., & Li, Q. (2009). Mantle convection controls the observed lateral variations in lithospheric thickness on present-day Mars. *Geophysical Research Letters*, 36, L18203. <https://doi.org/10.1029/2009GL039827>
- Kiefer, W. S., & Li, Q. (2016). Water undersaturated mantle plume volcanism on present-day Mars. *Meteoritics & Planetary Science*, 51(11), 1993–2010.
- Konopliv, A. S., Asmar, S. W., Folkner, W. M., Karatekin, Ö., Nunes, D. C., Smrekar, S. E., et al. (2011). Mars high resolution gravity fields from MRO, Mars seasonal gravity, and other dynamical parameters. *Icarus*, 211, 401–428. <https://doi.org/10.1016/j.icarus.2010.10.004>
- Konopliv, A. S., Park, R. S., & Folkner, W. M. (2016). An improved JPL Mars gravity field and orientation from Mars orbiter and lander tracking data. *Icarus*, 274(Supplement C), 253–260. <https://doi.org/10.1016/j.icarus.2016.02.052>
- Lainey, V. (2016). Quantification of tidal parameters from Solar System data. *Celestial Mechanics and Dynamical Astronomy*, 126, 145–156. <https://doi.org/10.1007/s10569-016-9695-y>
- Maurice, M., Tosi, N., Samuel, H., Plesa, A.-C., Hüttig, C., & Breuer, D. (2017). Onset of solid-state mantle convection and mixing during magma ocean solidification. *Journal of Geophysical Research: Planets*, 122, 577–598. <https://doi.org/10.1002/2016JE005250>

- McCubbin, F. M., Boyce, J. W., Srinivasan, P., Santos, A. R., Elardo, S. M., Filiberto, J., et al. (2016). Heterogeneous distribution of H<sub>2</sub>O in the martian interior: Implications for the abundance of H<sub>2</sub>O in depleted and enriched mantle sources. *Meteoritics & Planetary Science*, 51(11), 2036–2060.
- McNutt, M. K. (1984). Lithospheric flexure and thermal anomalies. *Journal of Geophysical Research*, 89(B13), 11,180–11,194. <https://doi.org/10.1029/JB089iB13p11180>
- Moore, W. B., & Schubert, G. (2000). Note: The tidal response of Europa. *Icarus*, 147, 317–319. <https://doi.org/10.1006/icar.2000.6460>
- Morschhauser, A., Grott, M., & Breuer, D. (2011). Crustal recycling, mantle dehydration, and the thermal evolution of Mars. *Icarus*, 212, 541–558. <https://doi.org/10.1016/j.icarus.2010.12.028>
- Musselwhite, D. S., Dalton, H. A., Kiefer, W. S., & Treiman, A. H. (2006). Experimental petrology of the basaltic shergottite Yamato-980459: Implications for the thermal structure of the martian mantle. *Meteoritics & Planetary Science*, 41(9), 1271–1290.
- Neukum, G., Jaumann, R., Hoffmann, H., Hauber, E., Head, J., Basilevsky, A., et al. (2004). Recent and episodic volcanic and glacial activity on Mars revealed by the high resolution stereo camera. *Nature*, 432, 971–979.
- Newsom, H. E., Crumpler, L. S., Reedy, R. C., Petersen, M. T., Newsom, G. C., Evans, L. G., et al. (2007). Geochemistry of martian soil and bedrock in mantled and less mantled terrains with gamma ray data from Mars Odyssey. *Journal of Geophysical Research*, 112, E03S12. <https://doi.org/10.1029/2006JE002680>
- Nimmo, F., & Faul, U. H. (2013). Dissipation at tidal and seismic frequencies in a melt-free, anhydrous Mars. *Journal of Geophysical Research: Planets*, 118, 2558–2569. <https://doi.org/10.1002/2013JE004499>
- Nimmo, F., & Tanaka, K. (2005). Early crustal evolution of Mars. *Annual Review of Earth and Planetary Sciences*, 33(1), 133–161. <https://doi.org/10.1146/annurev.earth.33.092203.122637>
- Padovan, S., Margot, J.-L., Hauck, S. A., Moore, W. B., & Solomon, S. C. (2014). The tides of Mercury and possible implications for its interior structure. *Journal of Geophysical Research: Planets*, 119, 850–866. <https://doi.org/10.1002/2013JE004459>
- Phillips, R. J., Zuber, M. T., Smrekar, S. E., Mellon, M. T., Head, J. W., Tanaka, K. L., et al. (2008). Mars north polar deposits: Stratigraphy, age, and geodynamical response. *Science*, 320(5880), 1182–1185. <https://doi.org/10.1126/science.1157546>
- Plesa, A.-C., & Breuer, D. (2014). Partial melting in one-plate planets: Implications for thermo-chemical and atmospheric evolution. *Planetary and Space Science*, 98, 50–65. <https://doi.org/10.1016/j.pss.2013.10.007>, planetary evolution and life.
- Plesa, A.-C., Grott, M., Tosi, N., Breuer, D., Spohn, T., & Wicczorek, M. A. (2016). How large are present-day heat flux variations across the surface of Mars? *Journal of Geophysical Research: Planets*, 121, 2386–2403. <https://doi.org/10.1002/2016JE005126>
- Plesa, A.-C., Tosi, N., & Breuer, D. (2014). Can a fractionally crystallized magma ocean explain the thermo-chemical evolution of Mars? *Earth and Planetary Science Letters*, 403, 225–235. <https://doi.org/10.1016/j.epsl.2014.06.034>
- Plesa, A. C., Tosi, N., Grott, M., & Breuer, D. (2015). Thermal evolution and Urey ratio of Mars. *Journal of Geophysical Research: Planets*, 120, 995–1010. <https://doi.org/10.1002/2014JE004748>
- Raterron, P., Holyoke, C., Tokle, L., Hilairet, N., Merkel, S., Hirth, G., & Weidner, D. (2017). Effect of iron content on olivine viscosity and implications for the Martian mantle. 48th. LPSC, The Woodlands, Texas, Abstract 1553.
- Rivoldini, A., Hoolst, T. V., Verhoeven, O., Mocquet, A., & Dehant, V. (2011). Geodesy constraints on the interior structure and composition of Mars. *Icarus*, 213(2), 451–472. <https://doi.org/10.1016/j.icarus.2011.03.024>
- Roberts, J., & Arkani-Hamed, J. (2017). Effects of basin-forming impacts on the thermal evolution and magnetic field of Mars. *Earth and Planetary Science Letters*, 478, 192–202. <https://doi.org/10.1016/j.epsl.2017.08.031>
- Roberts, J. H., & Zhong, S. (2006). Degree-1 convection in the martian mantle and the origin of the hemispheric dichotomy. *Journal of Geophysical Research*, 111, E06013. <https://doi.org/10.1029/2005JE002668>
- Ruedas, T., & Breuer, D. (2017). On the relative importance of thermal and chemical buoyancy in regular and impact-induced melting in a Mars-like planet. *Journal of Geophysical Research: Planets*, 122, 1554–1579. <https://doi.org/10.1002/2016JE005221>
- Ruedas, T., Tackley, P. J., & Solomon, S. C. (2013). Thermal and compositional evolution of the martian mantle: Effects of phase transitions and melting. *Physics of the Earth and Planetary Interiors*, 216, 32–58. <https://doi.org/10.1016/j.pepi.2012.12.002>
- Sautter, V., Toplis, M. J., Beck, P., Mangold, N., Wiens, R., Pinet, P., et al. (2016). Magmatic complexity on early Mars as seen through a combination of orbital, in-situ and meteorite data. *Lithos*, 254–255, 36–52. <https://doi.org/10.1016/j.lithos.2016.02.023>
- Schubert, G., & Spohn, T. (1990). Thermal history of Mars and the sulfur content of its core. *Journal of Geophysical Research*, 95(B9), 14,095–14,104. <https://doi.org/10.1029/JB095iB09p14095>
- Schumacher, S., & Breuer, D. (2006). Influence of a variable thermal conductivity on the thermochemical evolution of Mars. *Journal of Geophysical Research*, 111, E02006. <https://doi.org/10.1029/2007GL030083>
- Taylor, G. J., Boynton, W., Brückner, J., Wänke, H., Dreibus, G., Kerry, K., et al. (2006). Bulk composition and early differentiation of Mars. *Journal of Geophysical Research*, 111, E03S10. <https://doi.org/10.1029/2005JE002645>
- Thiriet, M., Michaut, C., Breuer, D., & Plesa, A.-C. (2018). Hemispheric dichotomy in lithosphere thickness on Mars caused by differences in crustal structure and composition. *Journal of Geophysical Research: Planets*, 123, 823–848. <https://doi.org/10.1002/2017JE005431>
- Tosi, N., Plesa, A.-C., & Breuer, D. (2013). Overturn and evolution of a crystallized magma ocean: A numerical parameter study for Mars. *Journal of Geophysical Research: Planets*, 118, 1512–1528. <https://doi.org/10.1002/jgre.20109>
- Tosi, N., Yuen, D. A., de Koker, N., & Wentzcovitch, R. M. (2013). Mantle dynamics with pressure- and temperature-dependent thermal expansivity and conductivity. *Physics of the Earth and Planetary Interiors*, 217, 48–58. <https://doi.org/10.1016/j.pepi.2013.02.004>
- Van Hoolst, T., Dehant, V., Roosbeek, F., & Lognonné, P. (2003). Tidally induced surface displacements, external potential variations, and gravity variations on Mars. *Icarus*, 161(2), 281–296. [https://doi.org/10.1016/S0019-1035\(02\)00045-3](https://doi.org/10.1016/S0019-1035(02)00045-3)
- Wänke, H., & Dreibus, G. (1994). Chemistry and accretion of Mars. *Philosophical Transactions of the Royal Society London*, A349, 2134–2137.
- Werner, S. C. (2009). The global martian volcanic evolutionary history. *Icarus*, 201, 44–68. <https://doi.org/10.1016/j.icarus.2008.12.019>
- Wicczorek, M. A. (2008). Constraints on the composition of the martian south polar cap from gravity and topography. *Icarus*, 196(2), 506–517. <https://doi.org/10.1016/j.icarus.2007.10.026>
- Wicczorek, M. A., Neumann, G. A., Nimmo, F., Kiefer, W. S., Taylor, G. J., Melosh, H. J., et al. (2013). The crust of the moon as seen by GRAIL. *Science*, 339(6120), 671–675. <https://doi.org/10.1126/science.1231530>
- Wicczorek, M. A., & Zuber, M. T. (2004). Thickness of the martian crust: Improved constraints from geoid-to-topography ratios. *Journal of Geophysical Research*, 109, E01009. <https://doi.org/10.1029/2003JE002153>
- Yoder, C. F., Konopliv, A. S., Yuan, D. N., Standish, E. M., & Folkner, W. M. (2003). Fluid core size of Mars from detection of the solar tide. *Science*, 300, 299–303. <https://doi.org/10.1126/science.1079645>
- Zhao, Y.-H., Zimmerman, M. E., & Kohlstedt, D. L. (2009). Effect of iron content on the creep behavior of olivine: 1. Anhydrous conditions. *Earth and Planetary Science Letters*, 287, 229–240. <https://doi.org/10.1016/j.epsl.2009.08.006>

- Zhong, S. (2009). Migration of Tharsis volcanism on Mars caused by differential rotation of the lithosphere. *Nature Geoscience*, 2, 19–23. <https://doi.org/10.1038/NGEO392>
- Zhong, S., & Roberts, J. H. (2003). On the support of the Tharsis Rise on Mars. *Earth and Planetary Science Letters*, 214(1), 1–9.
- Šrámek, O., & Zhong, S. (2012). Martian crustal dichotomy and Tharsis formation by partial melting coupled to early plume migration. *Journal of Geophysical Research*, 117, E01005. <https://doi.org/10.1029/2011JE003867>

**The thermal state and interior structure of Mars**

A.-C. Plesa<sup>1</sup>, S. Padovan<sup>1</sup>, N. Tosi<sup>1,2</sup>, D. Breuer<sup>1</sup>, M. Grott<sup>1</sup>, M. A. Wieczorek<sup>3</sup>,  
T. Spohn<sup>1</sup>, S. E. Smrekar<sup>4</sup>, W. B. Banerdt<sup>4</sup>

<sup>1</sup>German Aerospace Center (DLR), Rutherford Strasse 2, 12489 Berlin, Germany, <sup>2</sup>Technische Universität Berlin, Hardenberg Strasse 36 10623 Berlin, Germany, <sup>3</sup>Université Côte d'Azur, Observatoire de la Côte d'Azur, CNRS, Laboratoire Lagrange, France, <sup>4</sup>Jet Propulsion Laboratory, California Institute of Technology, 4800 Oak Grove Drive, Pasadena, CA 91109, USA.

**Contents of this file****Contents**

1. Thermal evolution model
2. Tidal model
3. Elastic lithosphere thickness model
4. Constraints on the interior of Mars
5. Crustal thickness variations
6. Crustal radioactivity and HPE distribution
7. Figures S1 to S8
8. Tables S1 to S3

**Additional Supporting Information (Files uploaded separately)**

1. Captions for Datasets S1 and S2

**Introduction**

In Section S1 we briefly describe the thermal evolution model used in this study. Section S2 describes the model used to compute the tidal parameters  $k_2$  and  $Q$  based on the temperature profiles obtained from the thermal evolution models. The method used to compute the elastic lithosphere thickness is described in Section S3. In Section S4 we discuss the data used to constrain the thermal evolution of Mars. Sections S5 and S6 provide additional discussion on the significance of variation of the crustal thickness and the crustal enrichment in heat producing elements. Figure S1 shows the evolution of the elastic lithosphere

thickness for the reference model (case 85 in Tables S1, S2 and S3). In Figure S2 we described the comparison of our temperatures to the estimated potential temperatures of the shergottites. Figure S3 shows histograms of the grain size obtained when using the reference viscosity of the thermal evolution models and the variation of  $k_2$  values when using different tide periods. Figures S4 and S5 shows temperature and viscosity profiles obtained in our simulations. Figure S6 shows a comparison of the present-day temperature profiles of the reference model with the martian solidus temperature of *Kiefer et al. (2015)* and *Ruedas and Breuer (2017)*. Figures S7 and S8 show the average surface heat flow compared to the heat flow value obtained at the InSight location and the elastic lithosphere thickness values obtained for the present-day north and south poles of Mars, respectively for each numerical simulation performed in this study. Table S1 lists the input parameters used in each individual model. In Table S2 we show the how well does each model fit the constraints employed in this study. Table S3 lists output parameters computed at present-day for each numerical simulation.

## S1 Thermal evolution model

Thermal evolution of the interior of Mars is modeled by using the mantle convection code Gaia (*Hüttig and Stemmer, 2008a,b; Hüttig et al., 2013*). We use a 3D spherical geometry and solve the conservation equations of mass, linear momentum and thermal energy, for which the non-dimensional form reads:

$$\nabla \cdot \vec{u} = 0, \quad (1)$$

$$\nabla \cdot [\eta(\nabla\vec{u} + (\nabla\vec{u})^T)] - \nabla p + (Ra\alpha T - \sum_{l=1}^3 Rb_l\Gamma_l)\vec{e}_r = 0, \quad (2)$$

$$\begin{aligned} \frac{DT}{Dt} - \nabla \cdot (k\nabla T) - Di\alpha(T + T_0)u_r - \frac{Di}{Ra}\Phi \\ - \sum_{l=1}^4 Di\frac{Rb_l}{Ra}\frac{D\Gamma_l}{Dt}\gamma_l(T + T_0) - H = 0, \end{aligned} \quad (3)$$

where  $\vec{u}$  is the velocity vector,  $\eta$  is the mantle viscosity,  $p$  is the dynamic pressure,  $\vec{e}_r$  is the unit vector in radial direction,  $k$  is the thermal conductivity,  $\alpha$  is the thermal expansivity,  $T$  is the temperature,  $u_r$  is the radial component of the velocity vector,  $Di$  is the dissipation number and  $\Phi \equiv \underline{\tau} : \underline{\dot{\epsilon}}/2$  is the viscous dissipation, where  $\underline{\tau}$  and  $\underline{\dot{\epsilon}}$  are the deviatoric stress and strain-rate tensors, respectively.  $Ra$ ,  $Rb_l$  and  $H$  are the thermal Rayleigh number, the Rayleigh number associated with the  $l$ -th phase transition, and the internal heating rate, respectively.

All our simulations use a mantle density of  $3500 \text{ kg/m}^3$  and employ crustal thickness models inferred from gravity and topography data with crustal densities between  $2700$  and  $3200 \text{ kg/m}^3$ . We do not consider chemical heterogeneities in the mantle, and for one crustal thickness model we use a lower density for the southern highlands (i.e.,  $2900 \text{ kg/m}^3$ ) compared to the northern lowlands (i.e.,  $3100 \text{ kg/m}^3$ ). The crust is enriched compared to the primitive mantle and has a blanketing effect due to its lower thermal conductivity. For a detailed description of the model we refer the reader to (*Plesa et al., 2015, 2016*).

Our models account for radioactive decay and core cooling during the  $4.5 \text{ Gyr}$  of thermal evolution. We note that all our models show temperatures at the core-mantle-boundary (CMB) that indicate a liquid core throughout the thermal evolution. A positive CMB heat

flow is obtained during the initial stage of evolution but decreases within the first 500 Myr to values below the critical heat flow necessary to power a thermal dynamo.

We use adiabatic heating and cooling of the mantle by assuming the extended Boussinesq Approximation (EBA). The thermal expansivity  $\alpha$  is assumed either constant or temperature- and pressure-dependent for which we use the parametrization of (*Tosi et al.*, 2013). Additionally, we include solid-solid phase transitions in the olivine and garnet-pyroxene system similar to (*Keller and Tackley*, 2009).

The mantle viscosity is temperature and pressure-dependent and follows an Arrhenius relation:

$$\eta(T, p) = \exp\left(\frac{E + pV}{T + T_0} - \frac{E + p_{ref}V}{T_{ref} + T_0}\right), \quad (4)$$

where  $E$  and  $V$  are the activation energy and activation volume, respectively. The non-dimensional surface temperature is given by  $T_0$ , while  $T_{ref}$  and  $p_{ref}$  are the reference temperature and pressure, respectively, at which the reference viscosity is attained. All our simulations use a reference temperature of 1600 K and a reference pressure of 3 GPa.

The mantle viscosity strongly decreases with increasing temperature but increases with increasing pressure. The activation energy controls the temperature dependence of the viscosity, while the activation volume its pressure dependence. Deformation experiments performed for diffusion creep indicate an activation energy of 300–375 kJ/mol (*Karato and Wu*, 1993; *Hirth and Kohlstedt*, 2003). The activation volume, however, is only poorly constrained and varies between 0 and 10 cm<sup>3</sup>/mol (*Hirth and Kohlstedt*, 2003). For a value of 0 cm<sup>3</sup>/mol the viscosity is purely temperature-dependent while an activation volume of 10 cm<sup>3</sup>/mol leads to a strong increase of viscosity with pressure (about one to three orders of magnitude for the pressure range of the martian mantle). In our simulations, to test the effects of the activation volume, we varied  $V$  between 0 and 20 cm<sup>3</sup>/mol (see Fig. S4 and S5).

## S2 Tidal model

The temperature field obtained from the convection simulations is horizontally averaged to provide a radial temperature profile. Using the parameters for the activation volume and reference viscosity for each model (Table 1) a grain size is computed assuming a linear rheology and additional experiment-based parameters (activation energy, prefactor) available in the literature (*Hirth and Kohlstedt*, 2003). The grain size  $d$  is obtained from the equation:

$$\dot{\epsilon} = A\sigma d^{-p} \exp\left(-\frac{E + pV}{RT}\right), \quad (5)$$

along with the relation  $\dot{\epsilon} = \sigma/\eta_{Ref}$ .

The temperature and pressure profiles, the activation volume, and the calculated grain-size are then used to compute the complex compliance using the Andrade pseudoperiod model (*Jackson et al.*, 2010; *Padovan et al.*, 2014). First, the complex compliance is calculated with (R and I indicate the real and imaginary part, respectively):

$$J_R = J_U \left[1 + \beta^* \Gamma(1 + n) \omega_a^{-n} \cos\left(\frac{n\pi}{2}\right)\right], \quad (6)$$

$$J_I = J_U \left[\beta^* \Gamma(1 + n) \omega_a^{-n} \sin\left(\frac{n\pi}{2}\right) + \frac{1}{\omega_v \tau_M}\right], \quad (7)$$

$$(8)$$

where  $J_U$  is the unrelaxed compliance (the inverse of the unrelaxed shear modulus  $G_U$ ),  $\Gamma$  is the gamma function and  $n$ ,  $\beta$ , and  $\tau_M$  are parameters of the Andrade creep function  $J(t) = J_U + \beta t^n + t/\eta$ . The effects of temperature, pressure, and timescale of the applied forcing enter the model through the frequency  $\omega_{v,a}$ , which is related to the pseudoperiod master variable  $X_B = 2\pi/\omega_{a,v}$ , through

$$X_B = T_0 \left( \frac{d}{d_{\text{Ref}}} \right)^{-m_{a,v}} \exp \left[ \left( -\frac{E}{R} \right) \left( \frac{1}{T} - \frac{1}{T_{\text{Ref}}} \right) \right] \exp \left[ \left( -\frac{V}{R} \right) \left( \frac{P}{T} - \frac{P_{\text{Ref}}}{T_{\text{Ref}}} \right) \right]. \quad (9)$$

The subscript Ref refers to the reference conditions (*Jackson et al.*, 2010),  $m_a$  ( $m_v$ ) is the grain size exponent for anelastic (viscous) processes,  $E$  is the activation energy,  $V$  the activation volume,  $R$  the gas constant, and  $T_0$  the period of the applied forcing. Values for parameters that are not included in the convection model (e.g.,  $\beta$ ,  $n$ ,  $m_{a,v}$ , etc.) are taken from *Jackson et al.* (2010). These parameters are based on olivine with an iron content lower than the martian mantle. We assume that the mantle is olivine-dominated and in computing the unrelaxed shear modulus  $G_U = 1/J_U$  we take  $\text{Mg}\# = 75$ . The high iron-content modifies the creep behaviour of olivine, by decreasing the viscosity by up to a factor of 10 (*Zhao et al.*, 2009). However, it is not possible to include consistently this effect in the model of *Jackson et al.* (2010), whose parameters are based on olivine with a different iron content. Thus, the  $Q$  calculated here can be seen as an upper value, since the effect of adding iron is to decrease the viscosity, which makes a given model more dissipative, and thus leads to a lower  $Q$  value. From the complex compliance the shear modulus  $G$  and viscosity  $\eta$  at a given depth in the mantle are obtained as

$$G = [J_R^2 + J_I^2]^{-0.5}, \quad (10)$$

$$\eta = \frac{1}{\omega J_I}. \quad (11)$$

The radial profiles of rigidity and viscosity are then used to calculate the complex Love number  $k_2^*$  using a matrix-propagator technique (e.g., *Moore and Schubert*, 2000; *Padovan et al.*, 2014). The elastic part  $k_2 = \Re(k_2^*)$  and the dissipation  $Q = k_2/\Im(k_2^*)$  can then be compared with values inferred from observations (*Genova et al.*, 2016; *Lainey*, 2016). We note that the value of  $Q$  reported in *Lainey* (2016) assumes that  $k_2$  is the same at the period of the semi-diurnal tides of the Sun and Phobos. This assumption is not accurate, since the rheological profile, and thus  $k_2$ , depends on the period  $T_0$  through the master variable  $X_B$ . However, we verified that  $k_2$  increases at most by 2% going from the period of the semi-diurnal tide of Phobos (5h33m) to the semi-diurnal Solar tide period (12h19m). We also note that the value of  $Q$  obtained by *Lainey* (2016) is based on the value of  $k_2$  of (*Konopliv et al.*, 2011). The correction required in using the most updated value from *Genova et al.* (2016) is below the 2% level.

### S3 Elastic lithosphere thickness model

The effective elastic thickness  $T_e$  is always smaller or equal to the mechanical lithosphere thickness  $D_m$ . The mechanical thickness represents a rheological boundary and, given a bounding stress, it defines the depth below which rocks loose their mechanical strength. For a given rheological model and using the yield strength envelope mechanism, the mechanical lithosphere thickness can be calculated based on an isotherm, which is associated with the onset of ductile deformation. The two quantities,  $T_e$  and  $D_m$  are similar if the lithospheric

plate has a small curvature and bending moment (*McNutt*, 1984). The geological features considered in this study show small curvatures and hence we consider  $T_e \simeq D_m$ .

We compute the elastic lithosphere thickness following the same procedure and using the same parameters as presented in (*Grott and Breuer*, 2008, 2010; *Plesa et al.*, 2016). We employ a bounding stress of  $\sigma_B = 10$  MPa (*Burov and Diament*, 1995; *Grott and Breuer*, 2010) to calculate the temperature at the base of the mechanical lithosphere:

$$T = \frac{E}{R} \left[ \log \left( \frac{\sigma_B^n A}{\dot{\epsilon}} \right) \right]^{-1}, \quad (12)$$

where  $E$  is the activation energy,  $R$  is the gas constant,  $A$  and  $n$  are rheological parameters and  $\dot{\epsilon}$  is the strain rate. Assuming a dislocation creep deformation mechanism, a strain rate of  $10^{-14} \text{ s}^{-1}$  representative for the deformation associated with the polar cap deposition on Mars (*Phillips et al.*, 2008) and a two layered system composed of a wet diabase crust and dry olivine mantle (*Grott and Breuer*, 2008), the temperatures that define the base of the mechanical thickness for the crust and mantle are 910 K and 1233 K, respectively. If instead we use a strain rate of  $10^{-17} \text{ s}^{-1}$  representative for deformation timescales associated with mantle convection, the temperatures at the base of the mechanical layer are 765 K and 1090 K for the crust and mantle, respectively.

If a weak crustal layer is present, the thicknesses of the elastic cores of the crust and mantle ( $T_{e,c}$  and  $T_{e,m}$ , respectively) are decoupled and the effective elastic thickness is calculated as follows:

$$T_e = (T_{e,m}^3 + T_{e,c}^3)^{\frac{1}{3}} \quad (13)$$

leading to a thin effective elastic thickness of the entire system. On the other hand, if an incompetent crustal layer is absent, the effective elastic thickness is calculated as the sum of the two components (mantle and crust), which act as a single elastic plate.

#### S4 Constraints on the interior of Mars

In the following we describe the observational data sets that we used to constrain the thermal state and interior structure of Mars.

The planetary tidal parameters  $k_2$  and  $Q$  are related to the interior structure and its rheological properties (e.g., *Nimmo and Faul*, 2013). For non-perfectly elastic bodies like Mars both the tidal Love number  $k_2$  and quality factor  $Q$  are frequency-dependent. The value of  $k_2$  refers to the period of the semi-diurnal Solar tide (*Van Hoolst et al.*, 2003; *Konopliv et al.*, 2016; *Genova et al.*, 2016).  $Q$  of Mars has been obtained from the observed acceleration of Phobos by assuming that  $k_2$  is the same at the frequency of the semi-diurnal Solar tide (12h19m) and at the period of the semi-diurnal tide of Phobos (5h33m) (*Lainey*, 2016). This assumption is acceptable given that  $k_2$  is predicted to increase only by up to 2% between the two periods (Fig. S2). The value of  $k_2$  depends strongly on the radius of the liquid core and to a lesser extent on the temperature of the mantle (e.g., *Yoder et al.*, 2003), while the value of  $Q$  depends mainly on the viscosity profile of the mantle (*Nimmo and Faul*, 2013). In this work, for each convection simulation, we use the present-day martian temperature field to compute a rheological profile and the corresponding values of  $k_2$  and  $Q$  (Section S2).

The effective elastic lithospheric thickness describes the response of lithospheric plates to long-term geological loading and is indicative of the thermal state of the mantle at the time at which the load was emplaced. Estimates of the elastic lithosphere thickness have been

derived from gravity and topography admittance studies, lithospheric flexure due to ice cap loading and rift flank uplift, as well as from the analysis of the brittle to ductile transition depth (see (*Grott et al.*, 2013) for a review), and are available at various times during the thermal evolution of Mars. We use the elastic lithosphere thickness estimates for the Noachian epoch (between 4.1 and 3.7 Gyr ago), where the elastic thickness is  $< 25$  km for the southern hemisphere. We do not take into account estimates for the Amazonian period (3.3 Gyr ago to present) because they are associated with very large timing uncertainties related to the build up of volcanic centers over billions of years. Nevertheless, we include the present-day elastic thickness estimates for the north and south pole regions of Mars. At the north pole, the thickness has been estimated to be larger than 300 km from the absence of lithospheric deflection below the ice cap as measured by the Shallow Radar instrument on board Mars Reconnaissance Orbiter (*Phillips et al.*, 2008). For the south pole, a localized spectral analysis combined with a lithospheric flexure model indicates that any value in excess of 110 km of the present-day elastic thickness can fit the observations, with a best-fit of 140 km *Wieczorek* (2008). A comparison of the elastic lithosphere thickness values obtained from our reference model with the available estimates is shown in Fig. S1.

Petrological analyses of martian meteorites and in-situ investigations performed by the martian rovers Spirit and Curiosity on surface rocks at Gusev and Gale craters, respectively, can be used to infer mantle potential temperatures and melt production in the interior at various ages during the evolution of the planet. Potential temperatures calculated by analyzing surface rocks from Gale crater, Gusev crater, and Meridiani Planum, and the clasts of the regolith breccia meteorite NWA7034 along with orbital spectrometry data of volcanic surfaces, indicate a cooling of the planet with time (e.g., *Filiberto and Dasgupta*, 2015). Despite the overall cooling, the potential temperatures obtained from ol-phyric shergottites at 472 and 180 Myr before present show high temperature values of 1813 and 1743 K, respectively. This has been interpreted to indicate the presence of positive thermal anomalies in the interior of Mars (*Filiberto and Dasgupta*, 2015), possibly related to hot mantle plumes, which could also be responsible for the recent volcanism identified from geological dating of surfaces in the Tharsis and Elysium volcanic provinces (*Hauber et al.*, 2011; *Neukum et al.*, 2004). Accordingly, successful models should locally exceed the solidus temperature (i.e., produce melt) at 472, 180 Myr ago and at present day.

The solidus temperature of the primitive martian mantle lies about 35 K lower than the terrestrial solidus (*Kiefer et al.*, 2015). We choose the martian solidus values of *Ruedas and Breuer* (2017, Appendix A), who used a lower terrestrial solidus and the same arguments of *Kiefer et al.* (2015) to derive the solidus temperature of the primitive martian mantle. The lower terrestrial value, which was used by *Ruedas and Breuer* (2017), has been found to better reproduce the experimental data (*Ruedas and Breuer*, 2017, Appendix A and references therein). Nevertheless, we acknowledge that the depletion of the mantle in crustal components have led to a solidus increase. The latter is taken into account by increasing the solidus linearly with the degree of depletion that each model should have experienced according to the crustal volume. The solidus of the depleted mantle for our best-fit cases lies close to the primitive solidus estimated by *Kiefer et al.* (2015). We note that only four best-fit cases including our reference model (cases 51, 85, 121, and 129) are found, if considering the depleted solidus of *Kiefer et al.* (2015). These four models represent a subset of the nine best-fit cases obtained when using the solidus of *Ruedas and Breuer* (2017). A comparison of the present-day temperature profiles of our reference case with the solidii of *Ruedas and Breuer* (2017) and *Kiefer et al.* (2015) is shown in Fig. S6. In addition to present-day melting, we require that successful models match at least one of the potential

temperatures inferred by petrological models of shergottites (Fig. S2).

## S5 Crustal thickness variations

We performed an additional calculation (case 86) to assess the importance of the crustal thickness distribution. Using the same parameters as the reference model, we tested whether models using a spatially-constant crustal thickness of 62 km can reproduce the observations. The thin crust over the southern hemisphere in case 86 with respect to the reference model (case 85) fails to produce enough insulation necessary to obtain a low elastic thickness during the Noachian epoch. At the same time the decreased insulation of the southern hemisphere in case 86 weakens the mantle plumes, which in turn cannot sustain partial melt production until recent times as required both by meteoritic samples and by geological mapping of large volcanic provinces.

## S6 Crustal Radioactivity and HPE distribution

The amount of heat producing elements in the crust compatible with the gamma-ray measurements indicate 275 pW/kg at 4.5 Gyr ago corresponding to a value of 49 pW/kg for the present-day crustal heat production rate (*Hahn et al.*, 2011). We compute the amount of heat producing elements in the mantle ( $H_m$ ) at 4.5 Gyr ago using a mass-balance calculation as follows:

$$H_m(M_{silicate} - M_{cr}) = H_0M_{silicate} - H_{cr}M_{cr} \quad (14)$$

$$H_m = \frac{H_0M_{silicate} - H_{cr}M_{cr}}{M_{silicate} - M_{cr}} \quad (15)$$

$$H_m = \frac{H_0\rho_m(R_p^3 - R_c^3) - H_{cr}\rho_{cr}(R_p^3 - R_{cr}^3)}{\rho_m(R_p^3 - R_c^3) - \rho_{cr}(R_p^3 - R_{cr}^3)}, \quad (16)$$

where  $M_{silicate}$  and  $M_{cr}$  are the total silicate mass and the mass of the crust, respectively,  $H_{cr}$  and  $H_0$  are the crustal amount of HPE and the bulk abundance of HPE at 4.5 Gyr ago, respectively,  $R_c$ ,  $R_{cr}$ , and  $R_p$  are the radius of the core, the radius at the base of the crust and the planetary radius, respectively, and  $\rho_{cr}$  and  $\rho_m$  are the density of the crust and the density of the mantle, respectively.

Since gamma-ray measurements can only map the topmost 10 cm of crust and the Th and K abundances in the martian meteorites are smaller than the values measured from orbit, the lower crustal layers might have a lower enrichment of HPE (*Newsom et al.*, 2007). Therefore, for a number of models, we assume a lower crustal heat production rate, which we varied to obtain values between 9.8 and 34.3 pW/kg at present day (i.e., 5 times to 1.4 times lower than the average value suggested by gamma-ray data) but use the bulk abundance of HPE consistent with the WD94 compositional model (*Wänke and Dreibus*, 1994). In such cases we observe a trade-off between the crustal thickness and the crustal enrichment in HPE. A thick crust of 87 km with a present-day crustal heat production rate  $H_{cr}$  of 49 pW/kg, which consistent with the average value suggested by gamma-ray measurements, can easily explain the large present-day elastic thickness at the north pole of Mars but has difficulties in matching the present-day south pole elastic thickness estimate due to decoupling of the elastic thicknesses of the mantle and crust (case 65). In addition, long standing volcanic activity is difficult to obtain for a mantle significantly depleted in HPE. On the other hand, an average crustal thickness of 87 km, which has a crustal heat production rate of only

9.8 pW/kg at present day (case 68) can explain the present-day elastic thickness value at the south pole but is not consistent with the north pole elastic thickness estimate.

To test the sensitivity of our results to the distribution of HPE, we performed additional calculations for which we systematically decreased the amount of HPE by reducing their value by 10 – 30% in the crust, in the mantle or in both mantle and crust for the reference model and a model with an average crustal thickness of only 45 km. We note that in these tests the bulk abundance of HPE is lower than the one inferred by the WD94 model (*Wänke and Dreibus, 1994*). If the crust is thin, and has an average thickness of 45 km, a decrease of crustal HPE by 20% or more leads to elastic thickness values during the Noachian larger than 25 km, while a decrease of HPE only in the mantle by 10% or more fails to produce recent melting in the mantle. However, if the crustal thickness is on average 62 km, a decrease of HPE in the mantle or crust by  $\leq 10\%$ , indicating a present-day crustal heat production rate of at least 44.1 pW/kg, can fit all observational constraints.

**Figure S1**

All successful models agree with small elastic thicknesses during the Noachian epoch and the present-day values for the north and south pole of Mars (full symbols). Other elastic thickness estimates are shown by transparent gray color, however, such estimates have not been used since they show large uncertainties. Here we show the evolution of the elastic lithosphere thickness for the reference case (case 85 in Tables 1, 2 and 3). The jump shown by the colored lines for the north and south pole is due to the fact that to compute  $T_e$  for the present-day north and south pole we use deformation timescales associated with the deposition of the polar caps (and hence a strain rate  $\dot{\epsilon}$  of  $10^{-14} \text{ s}^{-1}$ ), while for the evolution of the elastic thickness we use mantle convection timescales ( $\dot{\epsilon}$  of  $10^{-17} \text{ s}^{-1}$ ). The letters "N", "H", "NH", "HA" and "A" indicate Noachian, Hesperian, Noachian-Hesperian, Hesperian-Amazonian and Amazonian geological ages, respectively.

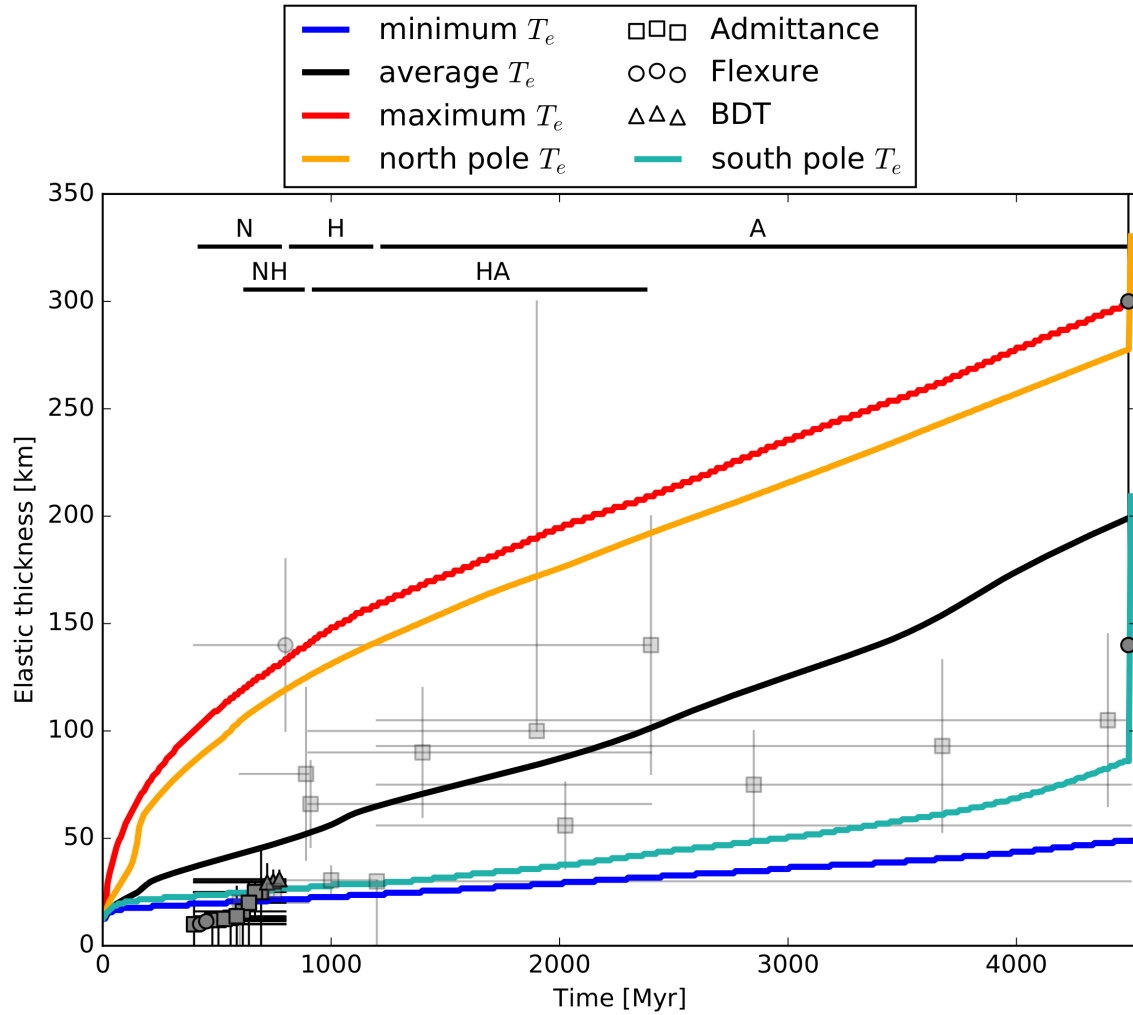


**Figure S2**

Temperature profile comparison to the potential temperatures of ol-phyric hergottites. Here we show the average temperature (black line) as well as minimum (blue line) and maximum (red line) temperature at each depth for our reference model (case 85 in Tables 1, 2 and 3).

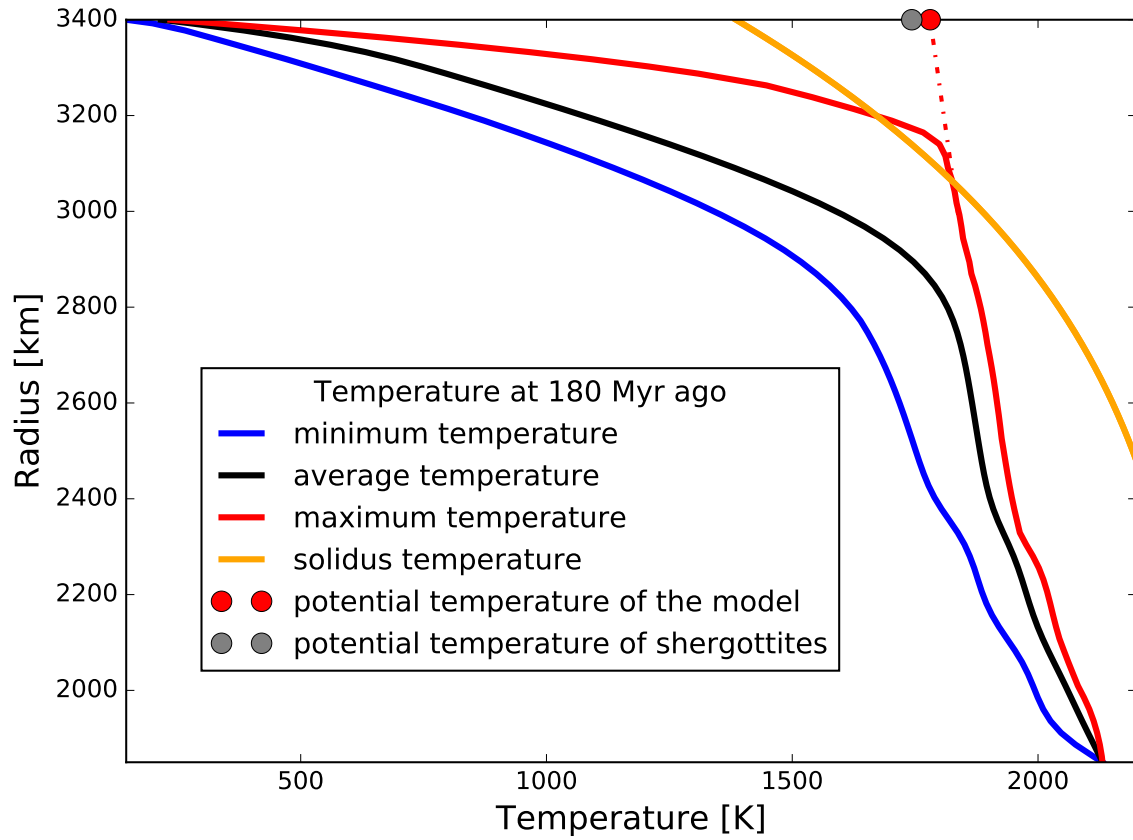


### Figure S3

For each thermal evolution model we compute the grain size according to the reference viscosity and other rheological parameters (Methods). Panel a) and b) show the results obtained when using an activation energy of 375 kJ/mol while the values in panels c) and d) have been obtained by using an activation energy of 325 kJ/mol. Panels a) and c) show a histogram of the obtained grain size values. Panels b) and d) show the variation of  $k_2$  values when using the semi-diurnal Solar tide period (12h19m) instead of the semi-diurnal period of the tide of Phobos (5h33m). The small variation of only up to < 2% supports the assumption that  $k_2$  is constant between the two periods.

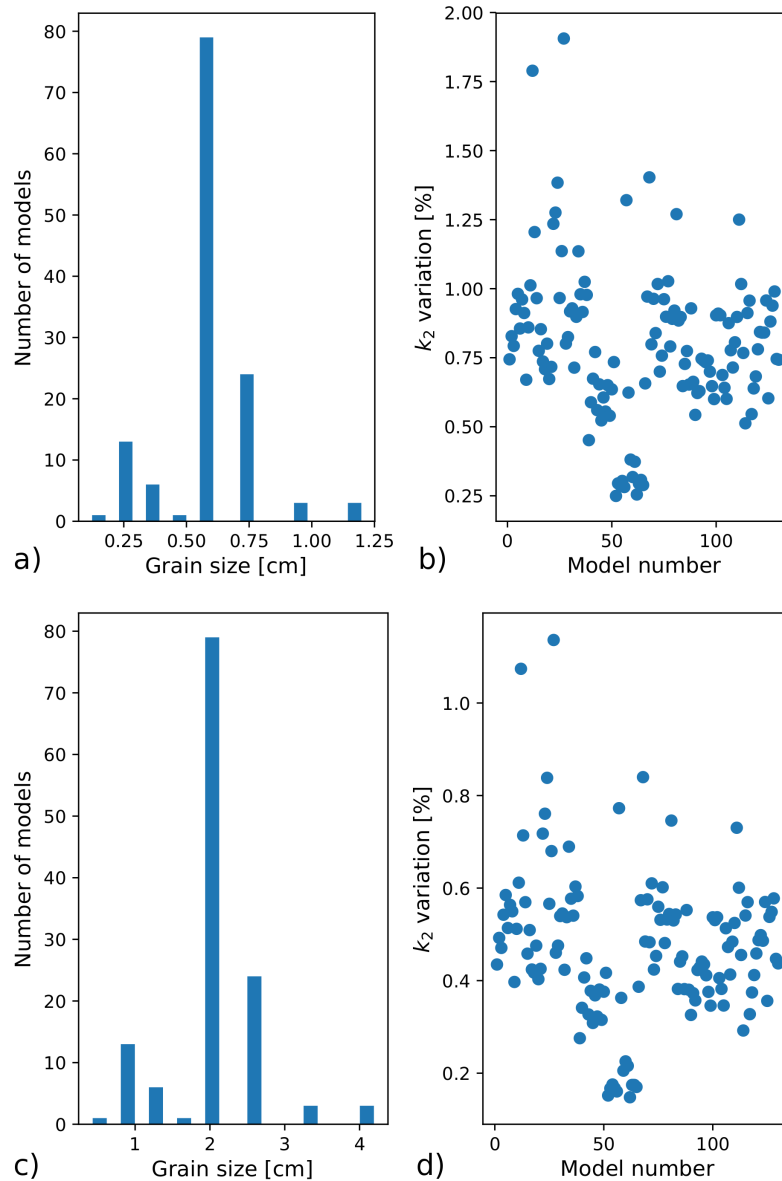


**Figure S4**

Average temperature profiles and corresponding temperature variations for two models using the same parameters but different activation volumes (cases 85 and 90 in Tables 1, 2 and 3) compared to a mantle adiabat (dashed line). The effects of the latent heat associated with solid-solid phase transformations is clearly visible for the model employing no pressure dependence of the viscosity. For all profiles presented here there is no perovskite layer at the base of the mantle.

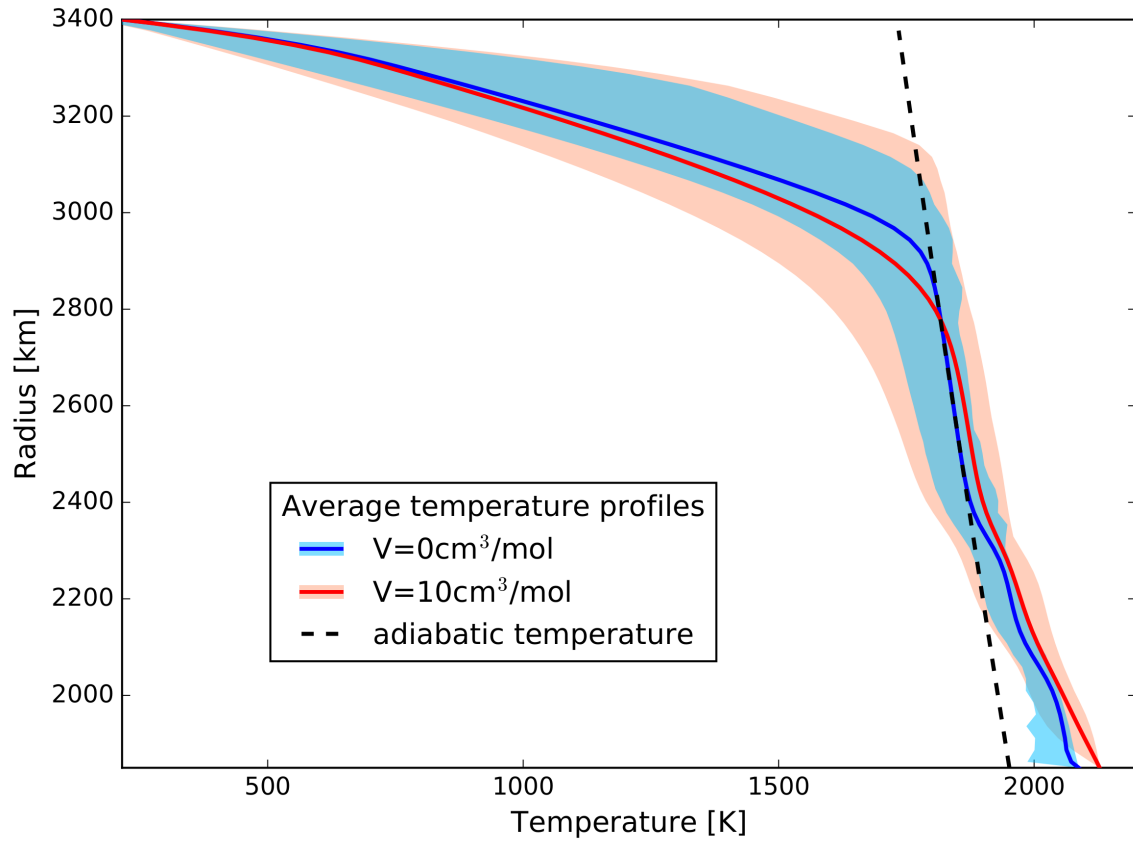


**Figure S5**

Evolution of the average viscosity profile for various simulations: a) case 89, which uses a lower activation volume ( $V = 6 \text{ cm}^3/\text{mol}$ ) compared to the reference case ( $V = 10 \text{ cm}^3/\text{mol}$ ), b) the reference case (case 85 in Tables 1, 2 and 3), c) case 91, which employs a lower reference viscosity ( $\eta_{ref} = 10^{20} \text{ Pa s}$ ) compared to the reference case ( $\eta_{ref} = 10^{21} \text{ Pa s}$ ) and d) case 121, which uses a higher temperature difference across the mantle ( $\Delta T = 2205 \text{ K}$ ) compared to the reference case ( $\Delta T = 2000 \text{ K}$ ). The present-day viscosity profile is shown by the dark red line. A reference viscosity of  $10^{21} \text{ Pa s}$  and a large activation volume of  $10 \text{ cm}^3/\text{mol}$  lead to limited cooling of the CMB temperature and hence to a small increase of the viscosity with time.

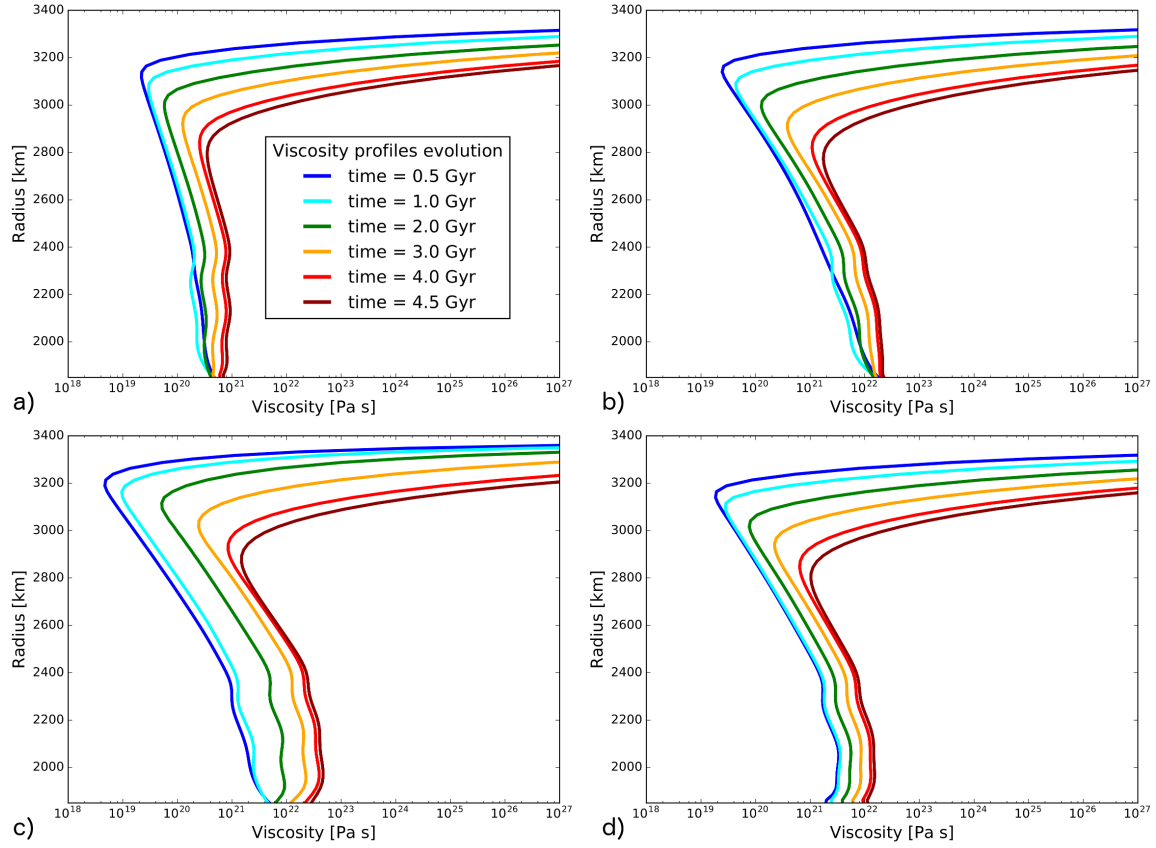


**Figure S6**

Comparison of the present-day temperature profiles of our reference case (case 85 in Tables 1, 2 and 3) with the solidus temperature values of *Ruedas and Breuer (2017)* and *Kiefer et al. (2015)*. The depleted solidus of *Ruedas and Breuer (2017)* has been obtained by increasing the primitive solidus of *Ruedas and Breuer (2017)* linearly with the degree of depletion, which has been estimated based on the crustal volume. The depleted solidus of *Kiefer et al. (2015)* has been obtained by increasing the primitive solidus of *Kiefer et al. (2015)* by 25 K (*Kiefer et al., 2015*). For further discussion see Section S4.

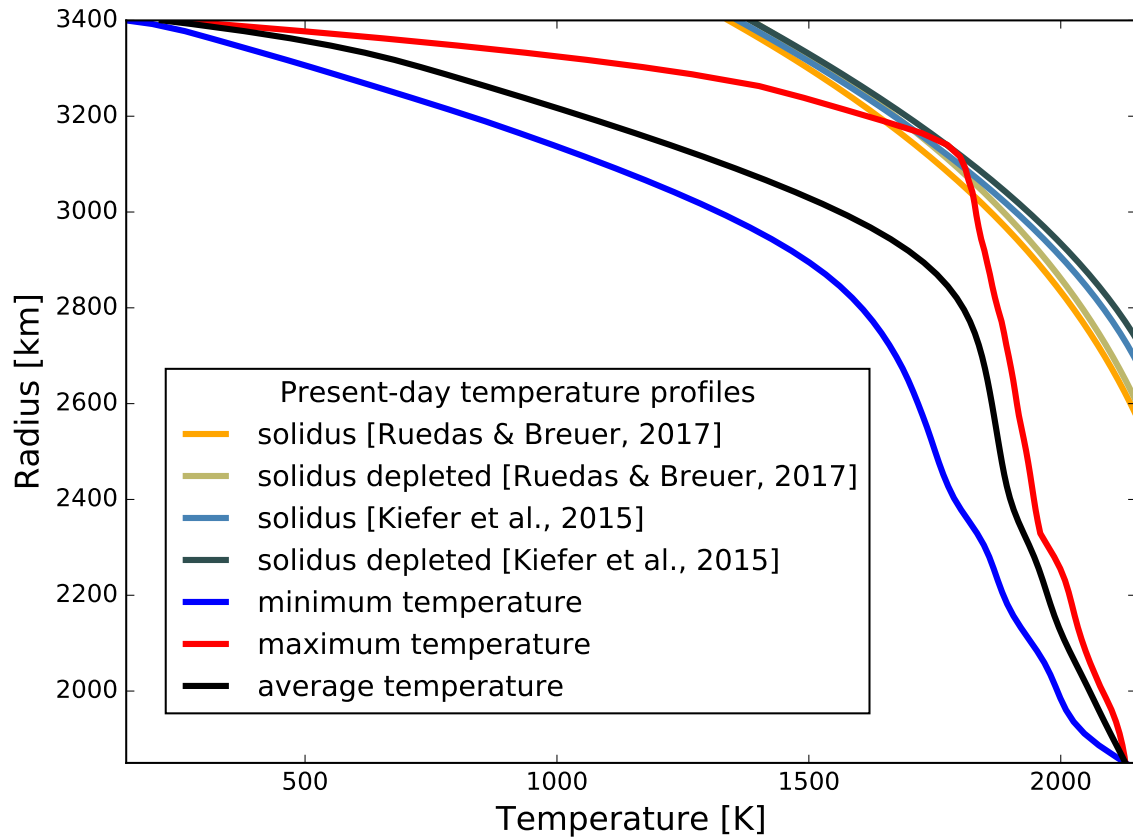


**Figure S7**

Average surface heat flow value compared to the heat flow value calculated at InSight landing site as obtained from all numerical simulations. The two values show a good correlation and differ by at most  $5 \text{ mW/m}^2$  for cases employing a high crustal density and hence a pronounced dichotomy in crustal thickness. In cases 94 – 108 we use a lower amount of HPE (by 10–30%, see Table 1) than the bulk abundance suggested by the WD94 compositional model (*Wänke and Dreibus, 1994*).

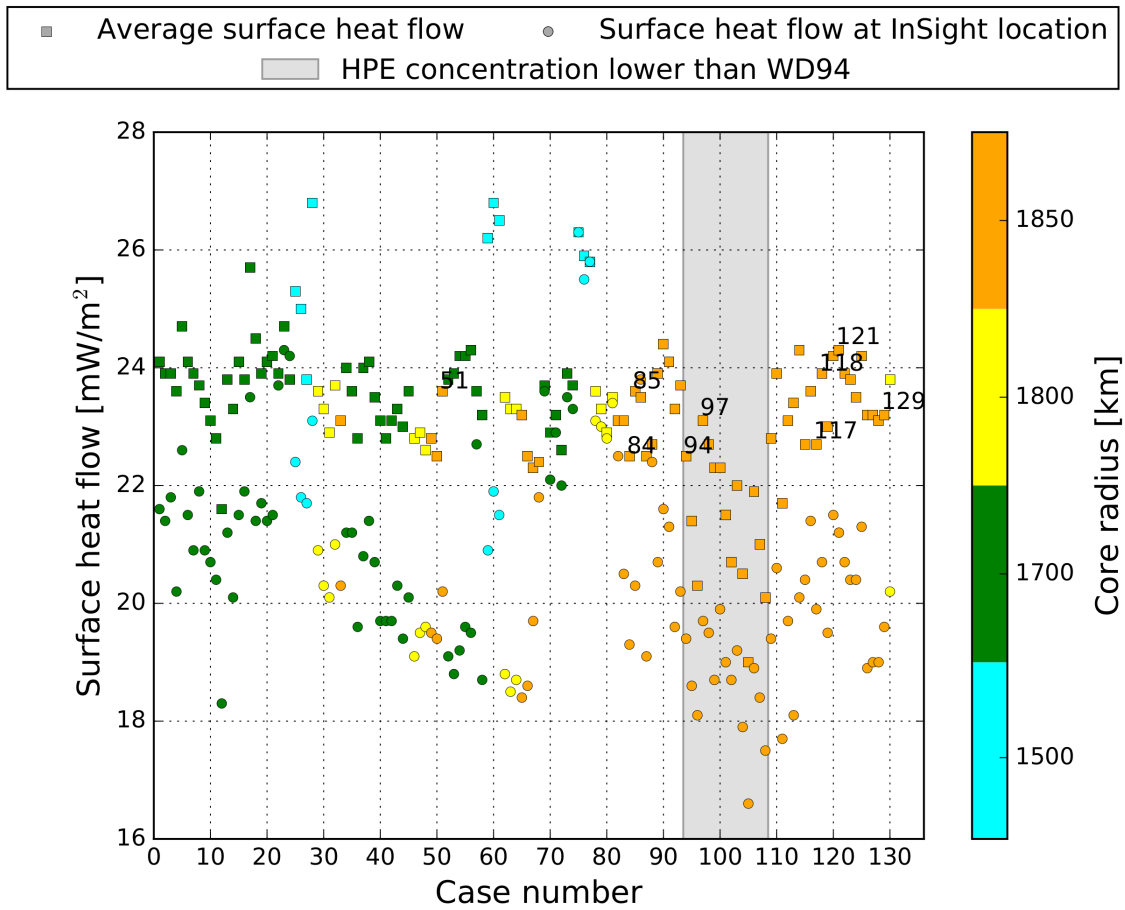


**Figure S8**

North and south pole elastic lithosphere thicknesses obtained in all numerical models together with the north and south pole estimates. While no cases employing a core radius of 1500 km and only a limited number of cases using a core radius of 1700 km satisfy both north and south pole elastic lithosphere thickness constraints, most cases with a core radius of 1850 km can fit the observations. Cases 94 – 108 use a lower concentration of heat producing elements than the one suggested by the WD94 compositional model (*Wänke and Dreibus, 1994*), which has been used in all other simulations.

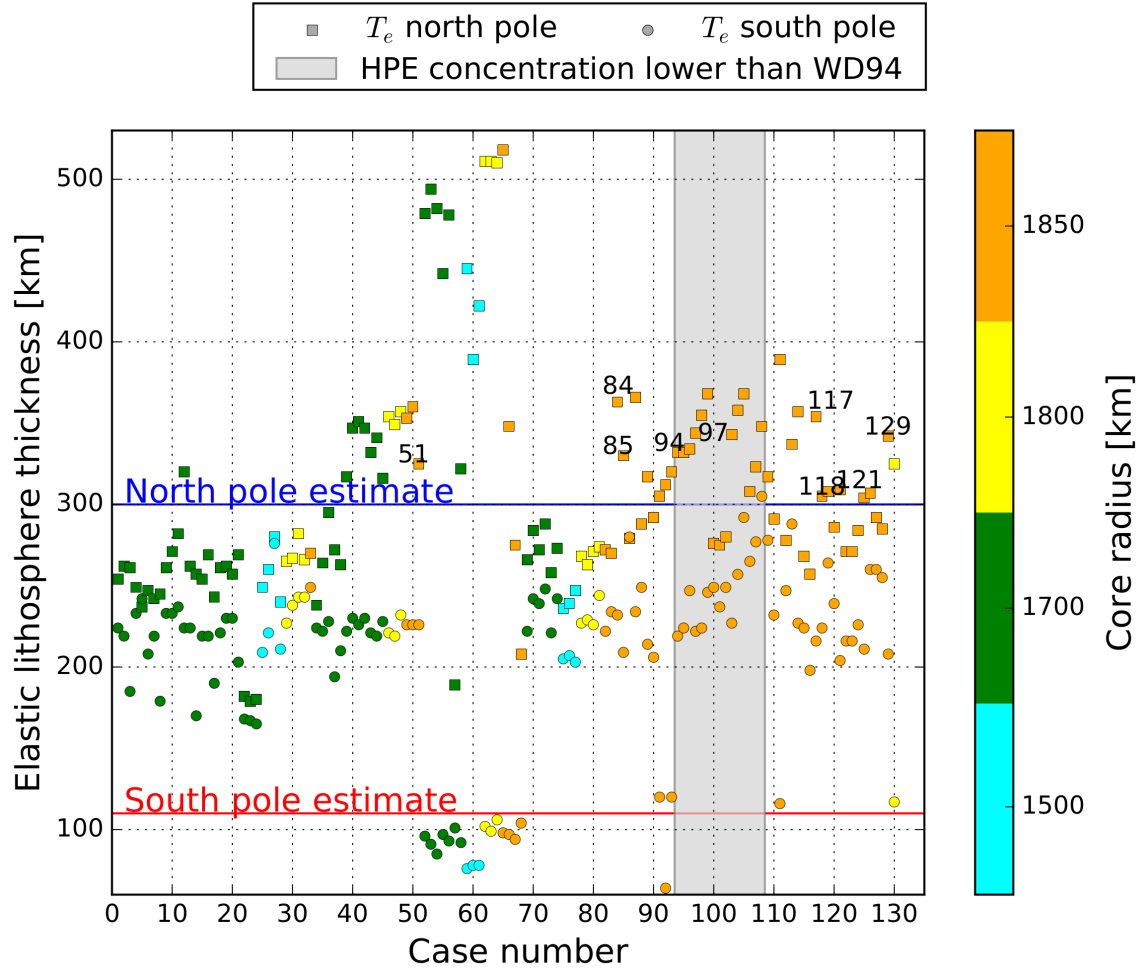


Table S1

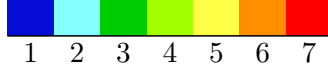
Input parameters for all simulations discussed in the text.  $R_c$  is the core radius,  $E$  is the activation energy,  $V$  is the activation volume,  $J$  is an additional viscosity jump in the mid mantle,  $\eta_{ref}$  is the reference viscosity,  $\alpha$  is the thermal expansivity,  $k_{cr}$  is the crust thermal conductivity,  $T_{init}$  is the initial mantle temperature,  $T_{surf}$  is the surface temperature,  $\Delta T$  is the temperature difference across the mantle,  $d_c$  is the average crustal thickness of the crustal thickness model that has been used,  $H_{cr}(0)$  and  $H_{cr}(today)$  are the crustal heat production rates at 4.5 Gyr ago and at present day.  $HPE_{cr}$  is the percentage of HPE located in the crust of the total HPE inventory, and was calculated as:  $100 \cdot (H_{cr} \cdot M_{cr}) / (H_{bulk} \cdot M_{silicate})$ , where  $H_{cr}$  and  $H_{bulk}$  are the heat production rate in the crust and the bulk inventory of HPE, respectively, while  $M_{cr}$  and  $M_{silicate}$  are the mass of the crust and the total silicate mass, respectively. The labels "0.7cHPE"–"0.9cHPE", "0.7mHPE"–"0.9mHPE" and "0.7HPE"–"0.9HPE" indicate a lower heat producing elements content in the crust, in the mantle, and in the mantle and crust, respectively compared to the WD94 compositional model.

Case	$R_c$ [km]	$V$ [cm <sup>3</sup> mol <sup>-1</sup> ]	$E$ [kJ mol <sup>-1</sup> ]	$J$ -	$\eta_{ref}$ [Pa s]	$\alpha$ [K <sup>-1</sup> ]	$k_{cr}$ [W m <sup>-1</sup> K <sup>-1</sup> ]	$T_{init}$ [K]	$T_{surf}$ [K]	$\Delta T$ [K]	$d_c$ [km]	$H_{cr}(0)$ [pW/kg]	$H_{cr}(today)$ [pW/kg]	$HPE_{cr}$ [%]	WD94 -
1	1700	3	300	-	10 <sup>21</sup>	2.5 × 10 <sup>-5</sup>	3	1650	var	2000	45.0	275	49	44.3	1
2	1700	6	300	-	10 <sup>21</sup>	2.5 × 10 <sup>-5</sup>	3	1650	var	2000	45.0	275	49	44.3	1
3	1700	6	300	50	10 <sup>21</sup>	2.5 × 10 <sup>-5</sup>	3	1650	var	2000	45.0	275	49	44.3	1
4	1700	10	300	-	10 <sup>21</sup>	2.5 × 10 <sup>-5</sup>	3	1650	var	2000	45.0	275	49	44.3	1
5	1700	10	300	-	10 <sup>21</sup>	2.5 × 10 <sup>-5</sup>	3	1850	var	2000	45.0	275	49	44.3	1
6	1700	6	300	-	10 <sup>21</sup>	2.5 × 10 <sup>-5</sup>	3	1650	216	2000	45.0	275	49	44.3	1
7	1700	10	300	-	10 <sup>21</sup>	2.5 × 10 <sup>-5</sup>	3	1650	216	2000	45.0	275	49	44.3	1
8	1700	10	300	-	10 <sup>21</sup>	2.5 × 10 <sup>-5</sup>	2	1650	var	2000	45.0	275	49	44.3	1
9	1700	0	300	-	10 <sup>21</sup>	$\alpha(p, T)$	3	1650	var	2000	45.0	275	49	44.3	1
10	1700	6	300	-	10 <sup>21</sup>	$\alpha(p, T)$	3	1650	var	2000	45.0	275	49	44.3	1
11	1700	10	300	-	10 <sup>21</sup>	$\alpha(p, T)$	3	1650	var	2000	45.0	275	49	44.3	1
12	1700	20	300	-	10 <sup>21</sup>	$\alpha(p, T)$	3	1650	var	2000	45.0	275	49	44.3	1
13	1700	10	300	-	10 <sup>21</sup>	$\alpha(p, T)$	3	1650	var	2340	45.0	275	49	44.3	1
14	1700	10	300	-	10 <sup>21</sup>	$\alpha(p, T)$	2	1650	var	2000	45.0	275	49	44.3	1
15	1700	6	300	-	5 × 10 <sup>20</sup>	2.5 × 10 <sup>-5</sup>	3	1650	var	2000	45.0	275	49	44.3	1
16	1700	10	300	-	5 × 10 <sup>20</sup>	2.5 × 10 <sup>-5</sup>	3	1650	var	2000	45.0	275	49	44.3	1
17	1700	6	300	-	10 <sup>20</sup>	2.5 × 10 <sup>-5</sup>	3	1650	var	2000	45.0	275	49	44.3	1
18	1700	6	300	50	10 <sup>20</sup>	2.5 × 10 <sup>-5</sup>	3	1650	var	2000	45.0	275	49	44.3	1
19	1700	10	300	-	10 <sup>20</sup>	2.5 × 10 <sup>-5</sup>	3	1650	var	2000	45.0	275	49	44.3	1
20	1700	6	300	-	10 <sup>20</sup>	$\alpha(p, T)$	3	1650	var	2000	45.0	275	49	44.3	1
21	1700	10	300	-	10 <sup>20</sup>	$\alpha(p, T)$	3	1650	var	2000	45.0	275	49	44.3	1
22	1700	3	300	-	10 <sup>21</sup>	2.5 × 10 <sup>-5</sup>	3	1650	var	2000	45.0	55	9.8	8.9	1
23	1700	6	300	-	10 <sup>21</sup>	2.5 × 10 <sup>-5</sup>	3	1650	var	2000	45.0	55	9.8	8.9	1
24	1700	10	300	-	10 <sup>21</sup>	2.5 × 10 <sup>-5</sup>	3	1650	var	2000	45.0	55	9.8	8.9	1
25	1500	6	300	-	10 <sup>21</sup>	$\alpha(p, T)$	3	1650	var	2000	45.0	275	49	42.4	1
26	1500	10	300	-	10 <sup>21</sup>	$\alpha(p, T)$	3	1650	var	2000	45.0	275	49	42.4	1
27	1500	20	300	-	10 <sup>21</sup>	$\alpha(p, T)$	3	1650	var	2000	45.0	275	49	42.4	1
28	1500	10	300	-	10 <sup>20</sup>	$\alpha(p, T)$	3	1650	var	2000	45.0	275	49	42.4	1
29	1800	6	300	-	10 <sup>21</sup>	2.5 × 10 <sup>-5</sup>	3	1650	var	2000	45.0	275	49	45.6	1
30	1800	10	300	-	10 <sup>21</sup>	2.5 × 10 <sup>-5</sup>	3	1650	var	2000	45.0	275	49	45.6	1
31	1800	10	300	-	10 <sup>21</sup>	$\alpha(p, T)$	3	1650	var	2000	45.0	275	49	45.6	1
32	1800	10	300	-	10 <sup>20</sup>	$\alpha(p, T)$	3	1650	var	2000	45.0	275	49	45.6	1
33	1850	10	300	-	10 <sup>21</sup>	2.5 × 10 <sup>-5</sup>	3	1650	var	2000	45.0	275	49	46.3	1
34	1700	10	300	-	10 <sup>21</sup>	2.5 × 10 <sup>-5</sup>	3	1650	var	2000	29.5	275	49	27.2	1
35	1700	10	300	-	10 <sup>21</sup>	2.5 × 10 <sup>-5</sup>	3	1650	var	2000	40.0	275	49	44.3	1
36	1700	10	300	-	10 <sup>21</sup>	2.5 × 10 <sup>-5</sup>	3	1650	var	2000	48.8	275	49	49.7	1
37	1700	10	300	-	10 <sup>21</sup>	2.5 × 10 <sup>-5</sup>	3	1850	var	2000	48.8	275	49	49.7	1
38	1700	10	300	-	10 <sup>21</sup>	$\alpha(p, T)$	3	1850	var	2000	48.8	275	49	49.7	1
39	1700	0	300	-	10 <sup>21</sup>	2.5 × 10 <sup>-5</sup>	3	1650	var	2000	62.0	275	49	65	1
40	1700	6	300	-	10 <sup>21</sup>	2.5 × 10 <sup>-5</sup>	3	1650	var	2000	62.0	275	49	65	1
41	1700	10	300	-	10 <sup>21</sup>	2.5 × 10 <sup>-5</sup>	3	1650	var	2000	62.0	275	49	65	1
42	1700	10	300	-	10 <sup>21</sup>	2.5 × 10 <sup>-5</sup>	3	1850	var	2000	62.0	275	49	65	1
43	1700	6	300	-	10 <sup>21</sup>	$\alpha(p, T)$	3	1650	var	2000	62.0	275	49	65	1
44	1700	10	300	-	10 <sup>21</sup>	$\alpha(p, T)$	3	1650	var	2000	62.0	275	49	65	1
45	1700	10	300	-	10 <sup>20</sup>	$\alpha(p, T)$	3	1650	var	2000	62.0	275	49	65	1
46	1800	10	300	-	10 <sup>21</sup>	$\alpha(p, T)$	3	1650	var	2000	62.0	275	49	66.8	1
47	1800	6	300	-	10 <sup>21</sup>	2.5 × 10 <sup>-5</sup>	3	1650	var	2000	62.0	275	49	66.8	1
48	1800	10	300	-	10 <sup>21</sup>	2.5 × 10 <sup>-5</sup>	3	1650	var	2000	62.0	275	49	66.8	1
49	1850	6	300	-	10 <sup>21</sup>	2.5 × 10 <sup>-5</sup>	3	1650	var	2000	62.0	275	49	67.8	1
50	1850	10	300	-	10 <sup>21</sup>	2.5 × 10 <sup>-5</sup>	3	1650	var	2000	62.0	275	49	67.8	1
51	1850	10	300	-	10 <sup>21</sup>	2.5 × 10 <sup>-5</sup>	3	1850	var	2000	62.0	275	49	67.8	1
52	1700	6	300	-	10 <sup>21</sup>	2.5 × 10 <sup>-5</sup>	3	1650	var	2000	87.1	275	49	93.5	1
53	1700	10	300	-	10 <sup>21</sup>	2.5 × 10 <sup>-5</sup>	3	1650	var	2000	87.1	275	49	93.5	1
54	1700	10	300	-	10 <sup>20</sup>	2.5 × 10 <sup>-5</sup>	3	1650	var	2000	87.1	275	49	93.5	1
55	1700	6	300	-	10 <sup>20</sup>	$\alpha(p, T)$	3	1650	var	2000	87.1	275	49	93.5	1
56	1700	10	300	-	10 <sup>20</sup>	$\alpha(p, T)$	3	1650	var	2000	87.1	275	49	93.5	1
57	1700	10	300	-	10 <sup>21</sup>	2.5 × 10 <sup>-5</sup>	3	1650	var	2000	87.1	55	9.8	18.7	1
58	1700	10	300	-	10 <sup>21</sup>	2.5 × 10 <sup>-5</sup>	3	1650	var	2000	87.1	192.5	34.3	65.5	1

59	1500	10	300	-	$10^{21}$	$2.5 \times 10^{-5}$	3	1650	var	2000	87.1	275	49	89.5	1
60	1500	6	300	-	$10^{20}$	$\alpha(p, T)$	3	1650	var	2000	87.1	275	49	89.5	1
61	1500	10	300	-	$10^{20}$	$\alpha(p, T)$	3	1650	var	2000	87.1	275	49	89.5	1
62	1800	6	300	-	$10^{21}$	$2.5 \times 10^{-5}$	3	1650	var	2000	87.1	275	49	96.1	1
63	1800	10	300	-	$10^{21}$	$2.5 \times 10^{-5}$	3	1650	var	2000	87.1	275	49	96.1	1
64	1800	10	300	-	$10^{21}$	$\alpha(p, T)$	3	1650	var	2000	87.1	275	49	96.1	1
65	1850	10	300	-	$10^{21}$	$2.5 \times 10^{-5}$	3	1650	var	2000	87.1	275	49	97.6	1
66	1850	10	300	-	$10^{21}$	$2.5 \times 10^{-5}$	3	1650	var	2000	87.1	192.5	34.3	68.3	1
67	1850	10	300	-	$10^{21}$	$2.5 \times 10^{-5}$	3	1650	var	2000	87.1	137.5	24.5	48.8	1
68	1850	10	300	-	$10^{21}$	$2.5 \times 10^{-5}$	3	1650	var	2000	87.1	55	9.8	19.5	1
69	1700	6	300	-	$10^{21}$	$2.5 \times 10^{-5}$	3	1650	var	2000	46.1	275	49	47	1
70	1700	10	300	-	$10^{21}$	$2.5 \times 10^{-5}$	3	1650	var	2000	46.1	275	49	47	1
71	1700	6	300	-	$10^{21}$	$\alpha(p, T)$	3	1650	var	2000	46.1	275	49	47	1
72	1700	10	300	-	$10^{21}$	$\alpha(p, T)$	3	1650	var	2000	46.1	275	49	47	1
73	1700	6	300	-	$10^{20}$	$\alpha(p, T)$	3	1650	var	2000	46.1	275	49	47	1
74	1700	10	300	-	$10^{20}$	$\alpha(p, T)$	3	1650	var	2000	46.1	275	49	47	1
75	1500	10	300	-	$10^{21}$	$2.5 \times 10^{-5}$	3	1650	var	2000	46.1	275	49	45	1
76	1500	6	300	-	$10^{21}$	$\alpha(p, T)$	3	1650	var	2000	46.1	275	49	45	1
77	1500	10	300	-	$10^{21}$	$\alpha(p, T)$	3	1650	var	2000	46.1	275	49	45	1
78	1800	6	300	-	$10^{21}$	$2.5 \times 10^{-5}$	3	1650	var	2000	46.1	275	49	48.3	1
79	1800	10	300	-	$10^{21}$	$2.5 \times 10^{-5}$	3	1650	var	2000	46.1	275	49	48.3	1
80	1800	10	300	-	$10^{21}$	$\alpha(p, T)$	3	1650	var	2000	46.1	275	49	48.3	1
81	1800	10	300	-	$10^{20}$	$\alpha(p, T)$	3	1650	var	2000	46.1	275	49	48.3	1
82	1850	10	300	-	$10^{21}$	$2.5 \times 10^{-5}$	3	1650	var	2000	46.1	275	49	49	1
83	1850	10	325	-	$10^{21}$	$2.5 \times 10^{-5}$	3	1850	var	2000	45.0	275	49	46.3	1
84	1850	10	325	-	$10^{21}$	$2.5 \times 10^{-5}$	3	1650	var	2000	62.0	275	49	67.8	1
85	1850	10	325	-	$10^{21}$	$2.5 \times 10^{-5}$	3	1850	var	2000	62.0	275	49	67.8	1
86	1850	10	325	-	$10^{21}$	$2.5 \times 10^{-5}$	3	1850	var	2000	62.0_avg	275	49	67.8	1
87	1850	10	375	-	$10^{21}$	$2.5 \times 10^{-5}$	3	1650	var	2000	62.0	275	49	67.8	1
88	1850	10	325	-	$10^{21}$	$2.5 \times 10^{-5}$	3	1650	var	2000	46.1	275	49	49	1
89	1850	6	325	-	$10^{21}$	$2.5 \times 10^{-5}$	3	1850	var	2000	62.0	275	49	67.8	1
90	1850	0	325	-	$10^{21}$	$2.5 \times 10^{-5}$	3	1850	var	2000	62.0	275	49	67.8	1
91	1850	10	325	-	$10^{20}$	$2.5 \times 10^{-5}$	3	1850	var	2000	62.0	275	49	67.8	1
92	1850	10	325	-	$10^{21}$	$2.5 \times 10^{-5}$	2	1850	var	2000	62.0	275	49	67.8	1
93	1850	10	325	-	$10^{21}$	$\alpha(p, T)$	3	1850	var	2000	62.0	275	49	67.8	1
94	1850	10	325	-	$10^{21}$	$2.5 \times 10^{-5}$	3	1850	var	2000	62.0	247.5	44.1	65.4	0.9cHPE
95	1850	10	325	-	$10^{21}$	$2.5 \times 10^{-5}$	3	1850	var	2000	62.0	220	39.2	62.7	0.8cHPE
96	1850	10	325	-	$10^{21}$	$2.5 \times 10^{-5}$	3	1850	var	2000	62.0	192.5	34.3	59.6	0.7cHPE
97	1850	10	325	-	$10^{21}$	$2.5 \times 10^{-5}$	3	1850	var	2000	62.0	275	49	70	0.9mHPE
98	1850	10	325	-	$10^{21}$	$2.5 \times 10^{-5}$	3	1850	var	2000	62.0	275	49	72.4	0.8mHPE
99	1850	10	325	-	$10^{21}$	$2.5 \times 10^{-5}$	3	1850	var	2000	62.0	275	49	75	0.7mHPE
100	1850	10	325	-	$10^{21}$	$2.5 \times 10^{-5}$	3	1650	var	2000	45.0	247.5	44.1	43.6	0.9cHPE
101	1850	10	325	-	$10^{21}$	$2.5 \times 10^{-5}$	3	1650	var	2000	45.0	220	39.2	40.8	0.8cHPE
102	1850	10	325	-	$10^{21}$	$2.5 \times 10^{-5}$	3	1650	var	2000	45.0	192.5	34.3	37.6	0.7cHPE
103	1850	10	325	-	$10^{21}$	$2.5 \times 10^{-5}$	3	1850	var	2000	62.0	247.5	44.1	67.8	0.9HPE
104	1850	10	325	-	$10^{21}$	$2.5 \times 10^{-5}$	3	1850	var	2000	62.0	220	39.2	67.8	0.8HPE
105	1850	10	325	-	$10^{21}$	$2.5 \times 10^{-5}$	3	1850	var	2000	62.0	192.5	34.3	67.8	0.7HPE
106	1850	10	325	-	$10^{21}$	$2.5 \times 10^{-5}$	3	1650	var	2000	45.0	275	49	48.9	0.9mHPE
107	1850	10	325	-	$10^{21}$	$2.5 \times 10^{-5}$	3	1650	var	2000	45.0	275	49	51.8	0.8mHPE
108	1850	10	325	-	$10^{21}$	$2.5 \times 10^{-5}$	3	1650	var	2000	45.0	275	49	55.1	0.7mHPE
109	1850	10	325	-	$10^{21}$	$2.5 \times 10^{-5}$	3	1650	var	2000	45.0	331.1	59	55.7	1
110	1850	10	325	-	$10^{21}$	$2.5 \times 10^{-5}$	3	1850	var	2000	45.0	331.1	59	55.7	1
111	1850	20	325	-	$10^{20}$	$2.5 \times 10^{-5}$	3	1850	var	2000	62.0	275	49	67.8	1
112	1850	10	325	-	$10^{21}$	$2.5 \times 10^{-5}$	3	1650	var	2000	29.5	385	68.6	39.7	1
113	1850	10	325	-	$10^{21}$	$2.5 \times 10^{-5}$	3	1650	var	2000	29.5	550	98	56.7	1
114	1850	10	325	-	$10^{21}$	$2.5 \times 10^{-5}$	3	1850	var	2000	62.0	331.1	59	81.6	1
115	1850	10	325	-	$10^{21}$	$2.5 \times 10^{-5}$	3	1650	var	2000	62.0	192.5	34.3	47.4	1
116	1850	10	325	-	$10^{21}$	$2.5 \times 10^{-5}$	3	1850	var	2000	62.0	192.5	34.3	47.4	1
117	1850	6	325	50	$10^{21}$	$2.5 \times 10^{-5}$	3	1650	var	2000	62.0	275	49	67.8	1
118	1850	6	325	50	$10^{21}$	$2.5 \times 10^{-5}$	3	1850	var	2000	62.0	275	49	67.8	1
119	1850	6	325	50	$10^{21}$	$2.5 \times 10^{-5}$	3	1650	var	2000	45.0	331.1	59	55.7	1
120	1850	6	325	50	$10^{21}$	$2.5 \times 10^{-5}$	3	1850	var	2000	45.0	331.1	59	55.7	1
121	1850	10	325	-	$10^{21}$	$2.5 \times 10^{-5}$	3	1850	var	2205	62.0	275	49	67.8	1
122	1850	6	325	-	$10^{21}$	$2.5 \times 10^{-5}$	3	1850	var	2000	48.8	275	49	51.8	1
123	1850	6	325	50	$10^{21}$	$2.5 \times 10^{-5}$	3	1850	var	2000	48.8	275	49	51.8	1
124	1850	10	325	-	$10^{21}$	$2.5 \times 10^{-5}$	3	1850	var	2000	48.8	275	49	51.8	1
125	1850	3	325	-	$10^{21}$	$2.5 \times 10^{-5}$	3	1850	var	2000	62.0	275	49	67.8	1
126	1850	10	325	-	$10^{21}$	$2.5 \times 10^{-5}$	3	1650	var	2000	29.5	467.5	83.3	48.2	1
127	1850	10	325	-	$10^{21}$	$2.5 \times 10^{-5}$	3	1650	var	2000	29.5	440	78.4	45.4	1
128	1850	10	325	-	$10^{21}$	$2.5 \times 10^{-5}$	3	1650	var	2000	29.5	412.5	73.5	42.5	1
129	1850	10	325	-	$10^{21}$	$2.5 \times 10^{-5}$	3	1650	var	2205	62.0	275	49	67.8	1
130	1800	10	325	-	$10^{21}$	$2.5 \times 10^{-5}$	3	1850	var	2000	62.0	275	49	66.8	1

**Table S2**

Fit of 7 constraints: dark blue represents a poor fit (just one constraint is met) while red shows a best fit (all constraints are met).



Summary of all constraints. ”+” means that the respective constraint is satisfied, while ”-” otherwise. The colored columns shows how many constrains are fulfilled (dark blue just one constraint, dark red all constraints). The last line shows how many cases are discarded by each constraint. The column ”fit1” shows how many cases are successful if  $T_{eNP}^{4.5Gyr} \geq 300$  km and the core radius is larger than 1850 km. Note that the cases indicated by a ”\*” in the case number use a higher crustal heat production rate than suggested by the gamma-ray data and are considered only marginally consistent with observations. The column ”fit2” shows how many cases show a best-fit if  $T_{eNP}^{4.5Gyr} \geq 280$  km and  $T_{eSP}^{4.5Gyr} \geq 100$  km. The column ”fit3” shows how many cases fit if we allow core radii of 1800 and 1700 km in addition to  $T_{eNP}^{4.5Gyr} \geq 280$  km and  $T_{eSP}^{4.5Gyr} \geq 100$  km.

Case	$T_e^{Noachian}$	$T_p^{shergottites}$	<i>Melting</i>	$T_{eNP}^{4.5Gyr}$	$T_{eSP}^{4.5Gyr}$	$k_2$	Q	fit1	fit2	fit3
1	+	+	+	-	+	-	+			
2	+	+	+	-	+	-	+			
3	+	+	+	-	+	-	+			
4	+	+	+	-	+	-	+			
5	+	+	+	-	+	-	+			
6	+	+	+	-	+	-	+			
7	+	+	+	-	+	-	+			
8	+	+	+	-	+	-	+			
9	+	-	-	-	+	-	+			
10	+	-	-	-	+	-	+			
11	+	-	-	-	+	-	-			
12	+	+	+	+	+	-	-			
13	+	+	+	-	+	-	-			
14	+	+	+	-	+	-	+			
15	+	+	+	-	+	-	+			
16	+	+	+	-	+	-	+			
17	+	-	-	-	+	-	+			
18	+	-	+	-	+	-	+			
19	+	-	+	-	+	-	+			
20	+	-	-	-	+	-	+			
21	+	-	+	-	+	-	+			
22	-	+	+	-	+	-	-			
23	-	+	+	-	+	-	-			
24	-	+	+	-	+	-	-			
25	+	+	-	-	+	-	-			
26	+	+	-	-	+	-	-			
27	+	+	+	-	+	-	-			
28	+	-	+	-	+	-	+			
29	+	+	+	-	+	-	+			

30	+	+	+	-	+	-	+		
31	+	+	-	-	+	-	+		
32	+	-	-	-	+	-	+		
33	+	+	+	-	+	+	+		
34	-	+	+	-	+	-	-		
35	+	+	+	-	+	-	+		
36	+	+	+	-	+	-	+		
37	+	+	+	-	+	-	-		
38	+	+	+	-	+	-	+		
39	+	-	-	+	+	-	-		
40	+	+	-	+	+	-	+		
41	+	+	+	+	+	-	+		
42	+	+	+	+	+	-	+		
43	+	-	-	+	+	-	+		
44	+	-	+	+	+	-	+		
45	+	-	+	+	+	-	+		
46	+	-	-	+	+	-	+		
47	+	-	-	+	+	-	+		
48	+	+	-	+	+	-	+		
49	+	-	-	+	+	+	+		
50	+	+	-	+	+	+	+		
51	+	+	+	+	+	+	+		
52	+	-	-	+	-	-	-		
53	+	+	+	+	-	-	-		
54	+	-	-	+	-	-	-		
55	+	-	-	+	-	-	-		
56	+	-	-	+	-	-	-		
57	-	+	+	-	-	-	-		
58	+	+	+	+	-	-	+		
59	+	-	+	+	-	-	-		
60	+	-	-	+	-	-	-		
61	+	-	-	+	-	-	-		
62	+	-	-	+	-	-	-		
63	+	-	-	+	-	-	-		
64	+	-	-	+	-	-	-		
65	+	-	-	+	-	-	-		
66	+	+	+	+	-	+	+		
67	-	+	+	-	-	+	-		
68	-	+	+	-	-	+	-		
69	+	+	+	-	+	-	+		
70	+	+	+	-	+	-	-		
71	+	+	+	-	+	-	+		
72	+	+	+	-	+	-	-		
73	+	-	-	-	+	-	+		
74	+	-	+	-	+	-	+		
75	+	+	+	-	+	-	+		
76	+	+	+	-	+	-	+		
77	+	+	+	-	+	-	+		

78	+	+	+	-	+	-	+	
79	+	+	+	-	+	-	+	
80	+	+	+	-	+	-	+	
81	+	-	-	-	+	+	+	
82	+	+	+	-	+	+	+	
83	+	+	+	-	+	+	+	
84	+	+	+	+	+	+	+	
85	+	+	+	+	+	+	+	
86	-	-	-	-	+	+	+	
87	+	-	-	+	+	+	+	
88	+	+	+	-	+	+	+	
89	+	+	-	+	+	+	+	
90	+	+	-	-	+	+	+	
91	+	-	+	+	+	+	+	
92	+	+	+	+	-	+	+	
93	+	-	+	+	+	+	+	
94	+	+	+	+	+	+	+	
95	+	+	-	+	+	+	+	
96	+	-	-	+	+	+	+	
97	+	+	+	+	+	+	+	
98	+	+	-	+	+	+	+	
99	+	+	-	+	+	+	+	
100	+	+	+	-	+	+	+	
101	-	+	+	-	+	+	+	
102	-	+	+	-	+	+	+	
103	+	+	-	+	+	+	+	
104	+	-	-	+	+	+	+	
105	+	-	-	+	+	+	+	
106	+	+	-	+	+	+	+	
107	+	-	-	+	+	+	+	
108	+	-	-	+	+	+	+	
109*	+	+	-	+	+	+	+	
110*	+	+	+	-	+	+	+	
111	+	-	+	+	+	+	-	
112*	+	+	+	-	+	+	-	
113*	+	-	-	+	+	+	+	
114*	+	+	+	+	+	+	-	
115	+	+	+	-	+	+	+	
116	+	+	+	-	+	+	-	
117	+	+	+	+	+	+	+	
118	+	+	+	+	+	+	+	
119*	+	+	-	+	+	+	+	
120*	+	+	+	-	+	+	+	
121	+	+	+	+	+	+	+	
122	+	+	+	-	+	+	+	
123	+	+	+	-	+	+	+	
124	+	+	+	-	+	+	-	
125	+	+	-	+	+	+	+	

126*	+	+	-	+	+	+	+			
127*	+	+	-	-	+	+	+			
128*	+	+	+	-	+	+	-			
129	+	+	+	+	+	+	+			
130	+	+	+	+	+	-	+			
Discarded cases	10	42	49	71	18	74	35	121	118	114

**Table S3**

Summary of results for all simulations discussed in the text. All values in columns 2–9 refer to the present-day.  $F_s$  [min, max], average surface heat flux with minimum and maximum values;  $T_e$  [min, max], average elastic thickness with minimum and maximum values calculated assuming a strain rate  $\dot{\epsilon} = 10^{-14} \text{ s}^{-1}$ ;  $F_s^{InSight}$ , surface heat flux at InSight location;  $T_e^{NP}$ , elastic lithosphere thickness averaged below the north pole ice cap (i.e., within  $10^\circ$  from the north pole);  $T_e^{SP}$ , elastic lithosphere thickness averaged below the south pole ice cap (i.e., within  $5^\circ$  from the south pole);  $T_{CMB}$ , core-mantle boundary temperature;  $F_{CMB}$ , core-mantle boundary heat flux;  $T_{mean}$  the average mantle temperature.

Case	$F_s$ [min, max] [mW m <sup>-2</sup> ]	$T_e$ [min, max] [km]	$F_s^{InSight}$ [mW m <sup>-2</sup> ]	$T_e^{NP}$ [km]	$T_e^{SP}$ [km]	$T_{CMB}$ [K]	$F_{CMB}$ [mW m <sup>-2</sup> ]	$T_{mean}$ [K]
1	24.1 [18.8, 31.1]	222 [ 91, 264]	21.6	254	224	2066.9	2.5	1627.2
2	23.9 [18.4, 32.0]	226 [ 83, 275]	21.4	262	219	2092.8	2.3	1629.0
3	23.9 [17.7, 30.2]	227 [101, 284]	21.8	261	185	2141.3	2.0	1622.9
4	23.6 [17.3, 31.0]	233 [ 97, 287]	20.2	249	233	2141.3	1.6	1622.5
5	24.7 [18.2, 32.6]	217 [ 81, 275]	22.6	237	242	2154.6	2.1	1642.9
6	24.1 [18.7, 32.7]	222 [ 84, 262]	21.5	247	208	2102.3	2.6	1636.5
7	23.9 [17.3, 32.4]	229 [ 86, 294]	20.9	242	219	2158.6	2.2	1629.7
8	23.7 [16.4, 34.4]	193 [ 44, 311]	21.9	245	179	2129.0	1.8	1655.0
9	23.4 [18.5, 30.0]	234 [ 105, 267]	20.9	261	233	2187.4	-0.3	1617.3
10	23.1 [17.8, 30.1]	240 [ 103, 282]	20.7	271	233	2209.3	-0.3	1622.2
11	22.8 [17.1, 30.4]	246 [ 99, 298]	20.4	282	237	2223.1	-0.4	1623.4
12	21.6 [15.5, 33.7]	281 [ 75, 350]	18.3	320	224	2247.8	-2.1	1624.1
13	23.8 [18.2, 31.5]	228 [ 89, 278]	21.2	262	224	2357.9	2.9	1666.1
14	23.3 [17.0, 32.5]	198 [ 48, 287]	20.1	257	170	2174.2	1.5	1658.9
15	24.1 [18.5, 32.5]	223 [ 81, 269]	21.5	254	219	2056.8	2.7	1605.5
16	23.8 [17.4, 36.1]	230 [ 66, 293]	21.9	269	219	2109.6	2.1	1596.1
17	25.7 [19.3, 51.3]	203 [ 42, 262]	23.5	243	190	1954.9	3.6	1545.7
18	24.5 [18.5, 34.6]	219 [ 73, 280]	21.4	261	221	2095.9	3.2	1558.5
19	23.9 [17.7, 33.8]	229 [ 75, 289]	21.7	262	230	2095.1	2.5	1554.7
20	24.1 [18.9, 31.3]	224 [ 94, 266]	21.4	257	230	2032.9	3.4	1550.8
21	24.2 [17.6, 39.3]	226 [ 60, 294]	21.5	269	203	2071.0	3.0	1541.1
22	23.9 [22.4, 25.2]	166 [ 88, 188]	23.7	182	168	2172.1	2.5	1763.7
23	24.7 [22.3, 26.9]	160 [ 81, 188]	24.3	179	167	2181.7	3.6	1762.1
24	23.8 [21.1, 28.1]	169 [ 87, 201]	24.2	180	165	2215.2	2.3	1746.4
25	25.3 [19.5, 33.4]	217 [ 82, 258]	22.4	249	209	2247.2	-1.4	1689.4
26	25.0 [18.6, 34.2]	222 [ 77, 274]	21.8	260	221	2260.0	-1.5	1689.5
27	23.8 [16.9, 52.1]	254 [ 42, 328]	21.7	280	276	2269.1	-2.7	1684.2
28	26.8 [19.7, 44.6]	200 [ 50, 260]	23.1	240	211	2128.6	2.4	1599.0
29	23.6 [18.2, 31.9]	231 [ 85, 277]	20.9	265	227	2066.4	2.6	1606.3
30	23.3 [17.1, 31.8]	238 [ 86, 299]	20.3	267	238	2118.9	2.0	1599.8
31	22.9 [17.1, 30.1]	244 [ 101, 297]	20.1	282	243	2155.8	1.8	1597.7
32	23.7 [17.4, 32.6]	233 [ 84, 297]	21.0	266	243	2041.1	3.2	1519.5
33	23.1 [17.0, 32.2]	241 [ 84, 303]	20.3	270	249	2106.8	2.2	1587.0
34	24.0 [20.1, 30.9]	207 [149, 251]	21.2	238	224	2176.1	1.8	1676.4
35	23.6 [18.1, 31.1]	225 [ 97, 280]	21.2	264	222	2150.3	1.7	1639.8

36	22.8	[16.5, 33.5]	250	[ 77, 316]	19.6	295	228	2184.4	0.6	1607.7
37	24.0	[17.5, 34.7]	229	[ 71, 291]	20.8	272	194	2215.5	1.1	1638.0
38	24.1	[17.7, 34.2]	227	[ 72, 282]	21.4	263	210	2194.9	2.1	1633.0
39	23.5	[15.4, 34.3]	258	[ 71, 329]	20.7	317	222	2069.9	1.3	1545.0
40	23.1	[14.5, 35.3]	272	[ 68, 358]	19.7	347	230	2109.9	1.4	1543.4
41	22.8	[14.1, 36.1]	282	[ 66, 381]	19.7	351	226	2133.2	0.8	1539.9
42	23.1	[14.5, 35.3]	272	[ 68, 358]	19.7	347	230	2109.9	1.4	1543.4
43	23.3	[15.0, 34.8]	265	[ 69, 345]	20.3	332	221	2074.4	2.1	1544.1
44	23.0	[13.9, 36.5]	277	[ 66, 390]	19.4	341	219	2117.7	1.5	1538.5
45	23.6	[14.2, 41.3]	264	[ 56, 392]	20.1	316	228	2028.7	2.8	1476.9
46	22.8	[13.7, 34.9]	283	[ 69, 397]	19.1	354	221	2094.1	1.9	1514.2
47	22.9	[14.3, 35.1]	276	[ 69, 367]	19.5	349	219	2089.2	1.8	1519.3
48	22.6	[13.8, 35.7]	287	[ 67, 387]	19.6	357	232	2111.7	1.3	1515.1
49	22.8	[14.1, 34.9]	279	[ 69, 369]	19.5	353	226	2074.2	1.9	1506.1
50	22.5	[13.8, 35.5]	290	[ 68, 389]	19.4	360	226	2098.7	1.5	1502.2
51	23.6	[14.4, 37.7]	262	[ 62, 372]	20.2	325	226	2129.0	2.0	1540.1
52	23.8	[10.9, 37.4]	310	[ 63, 523]	19.1	479	96	2004.3	2.2	1419.8
53	23.9	[10.7, 38.5]	319	[ 61, 547]	18.8	494	91	2031.7	2.2	1413.3
54	24.2	[10.8, 37.6]	305	[ 63, 550]	19.2	482	85	1988.7	2.7	1387.8
55	24.2	[11.7, 35.8]	290	[ 67, 484]	19.6	442	97	1967.0	3.0	1400.4
56	24.3	[10.9, 37.7]	298	[ 63, 540]	19.5	478	93	1978.4	2.9	1385.8
57	23.6	[19.8, 30.0]	135	[ 71, 221]	22.7	189	101	2199.9	2.1	1740.5
58	23.2	[12.8, 35.9]	222	[ 63, 410]	18.7	322	92	2090.3	1.7	1561.8
59	26.2	[11.9, 41.0]	270	[ 57, 488]	20.9	445	76	2060.4	0.7	1485.0
60	26.8	[13.2, 38.4]	237	[ 62, 425]	21.9	389	78	2011.8	1.4	1467.4
61	26.5	[12.3, 38.6]	253	[ 62, 472]	21.5	422	78	2058.5	1.1	1459.7
62	23.5	[10.6, 37.2]	329	[ 64, 549]	18.8	511	102	2030.3	1.8	1388.0
63	23.3	[10.5, 37.9]	339	[ 62, 549]	18.5	511	99	2037.7	1.9	1388.1
64	23.3	[10.6, 36.7]	339	[ 65, 544]	18.7	510	106	2040.6	1.7	1386.8
65	23.2	[10.4, 37.8]	343	[ 62, 559]	18.4	518	98	2029.0	2.2	1375.2
66	22.5	[12.6, 33.1]	239	[ 70, 414]	18.6	348	97	2098.9	1.6	1530.0
67	22.3	[15.3, 29.8]	193	[ 77, 316]	19.7	275	94	2155.1	1.5	1616.3
68	22.4	[19.3, 25.0]	147	[ 85, 222]	21.8	208	104	2233.1	1.6	1716.8
69	23.7	[18.1, 35.9]	230	[ 66, 280]	23.6	266	222	2086.5	2.3	1619.9
70	22.9	[16.8, 35.8]	246	[ 66, 309]	22.1	284	242	2193.2	0.5	1617.6
71	23.2	[17.7, 34.3]	238	[ 71, 280]	22.9	272	239	2154.6	1.6	1618.9
72	22.6	[16.8, 34.6]	252	[ 70, 305]	22.0	288	248	2217.0	-0.5	1618.9
73	23.9	[18.6, 35.1]	228	[ 68, 269]	23.5	258	221	2050.1	3.1	1551.9
74	23.7	[17.4, 39.9]	234	[ 57, 296]	23.3	273	242	2083.6	2.7	1542.2
75	26.3	[19.3, 41.5]	204	[ 57, 268]	26.3	236	205	2187.2	1.1	1680.2
76	25.9	[19.9, 38.1]	207	[ 63, 247]	25.5	239	207	2222.5	1.5	1687.2
77	25.8	[19.2, 38.0]	210	[ 63, 266]	25.8	247	203	2233.1	0.7	1685.5
78	23.6	[17.7, 35.6]	232	[ 67, 283]	23.1	268	227	2064.0	2.5	1603.3
79	23.3	[16.9, 38.3]	239	[ 61, 302]	23.0	263	229	2117.5	1.9	1595.8
80	22.9	[17.2, 35.5]	244	[ 67, 299]	22.8	271	226	2153.6	1.8	1594.7
81	23.5	[17.4, 36.8]	236	[ 64, 299]	23.4	274	244	2044.4	3.1	1519.1
82	23.1	[16.9, 36.4]	242	[ 65, 310]	22.5	272	222	2106.0	2.1	1583.4
83	23.1	[17.2, 32.3]	241	[ 82, 298]	20.5	270	234	2101.0	2.1	1589.1

84	22.5	[13.8, 36.4]	291	[ 65, 391]	19.3	363	232	2098.7	1.5	1503.9
85	23.6	[14.7, 36.6]	262	[ 65, 359]	20.3	330	209	2128.2	2.0	1542.3
86	23.5	[22.8, 24.4]	266	[ 239, 298]	23.8	279	280	2137.0	1.9	1548.1
87	22.5	[13.8, 34.5]	290	[ 71, 384]	19.1	366	234	2098.5	1.4	1506.7
88	22.7	[16.8, 35.3]	248	[ 68, 308]	22.4	288	249	2158.1	1.3	1586.3
89	23.9	[15.5, 35.7]	251	[ 67, 330]	20.7	317	214	2113.2	2.7	1550.8
90	24.4	[16.5, 35.0]	238	[ 69, 302]	21.6	292	206	2087.2	1.5	1561.5
91	24.1	[15.0, 38.2]	253	[ 62, 356]	21.3	305	120	2029.7	3.5	1482.1
92	23.2	[13.2, 35.1]	196	[ 44, 415]	19.6	312	64	2043.9	2.4	1562.6
93	23.7	[14.9, 37.3]	257	[ 63, 353]	20.2	320	120	2111.4	2.7	1544.4
94	22.5	[14.3, 34.1]	267	[ 70, 364]	19.4	332	219	2129.7	1.9	1537.9
95	21.4	[14.1, 32.3]	273	[ 74, 363]	18.6	332	224	2130.5	1.9	1533.3
96	20.3	[14.1, 28.7]	278	[ 86, 358]	18.1	334	247	2131.1	1.9	1528.7
97	23.1	[14.2, 35.8]	273	[ 67, 372]	19.7	344	222	2120.0	1.9	1525.8
98	22.7	[13.7, 34.7]	284	[ 70, 392]	19.5	355	224	2111.5	2.0	1508.4
99	22.3	[13.2, 35.8]	296	[ 67, 410]	18.7	368	246	2103.3	2.0	1490.8
100	22.3	[17.1, 31.7]	243	[ 81, 293]	19.9	276	249	2101.7	2.1	1586.7
101	21.5	[16.8, 29.0]	245	[ 94, 297]	19.0	275	237	2103.2	2.0	1584.3
102	20.7	[16.3, 26.5]	248	[ 115, 298]	18.7	280	249	2104.1	2.1	1582.0
103	22.0	[13.9, 33.0]	278	[ 74, 372]	19.2	343	227	2121.3	1.9	1520.9
104	20.5	[13.4, 30.9]	296	[ 79, 387]	17.9	358	257	2114.1	1.9	1498.3
105	19.0	[12.9, 27.7]	315	[ 90, 387]	16.6	368	292	2106.9	1.8	1474.5
106	21.9	[16.0, 30.5]	265	[ 99, 321]	18.9	308	265	2146.3	1.3	1562.5
107	21.0	[15.2, 28.9]	284	[ 118, 343]	18.4	323	277	2132.3	1.3	1533.3
108	20.1	[14.5, 28.3]	306	[ 134, 363]	17.5	348	305	2118.5	1.3	1502.1
109	22.8	[16.0, 33.4]	275	[ 87, 338]	19.4	317	278	2134.4	1.3	1545.8
110	23.9	[17.0, 34.2]	253	[ 81, 311]	20.6	291	232	2160.4	1.8	1577.0
111	21.7	[12.7, 46.4]	333	[ 48, 433]	17.7	389	116	2172.3	0.5	1468.7
112	23.1	[18.5, 31.1]	246	[ 185, 287]	19.7	278	247	2175.4	1.2	1600.6
113	23.4	[17.5, 34.1]	297	[ 216, 348]	18.1	337	288	2129.9	1.2	1518.5
114	24.3	[13.0, 41.8]	293	[ 57, 445]	20.1	357	227	2039.4	2.7	1475.2
115	22.7	[16.1, 34.1]	226	[ 67, 306]	20.4	268	224	2095.3	2.1	1599.0
116	23.6	[16.8, 32.1]	212	[ 73, 290]	21.4	257	198	2110.2	2.6	1617.6
117	22.7	[13.7, 35.5]	282	[ 68, 394]	19.9	354	216	2098.4	2.0	1505.4
118	23.9	[14.9, 35.9]	253	[ 67, 356]	20.7	305	224	2133.3	2.3	1547.5
119	23.0	[16.0, 32.7]	268	[ 94, 335]	19.5	308	264	2134.8	1.8	1545.8
120	24.2	[17.3, 34.7]	245	[ 78, 302]	21.5	286	239	2165.2	2.3	1580.8
121	24.3	[14.9, 36.4]	245	[ 66, 354]	21.2	309	204	2175.9	3.4	1571.6
122	23.9	[17.9, 33.0]	231	[ 79, 282]	20.7	271	216	2158.3	2.5	1604.1
123	23.8	[17.5, 33.0]	232	[ 79, 292]	20.4	271	216	2178.0	2.3	1602.4
124	23.5	[17.2, 33.8]	239	[ 75, 297]	20.4	284	226	2172.2	2.0	1598.0
125	24.2	[16.1, 35.3]	244	[ 68, 316]	21.3	304	211	2099.3	2.6	1557.2
126	23.2	[18.1, 32.8]	269	[ 196, 318]	18.9	307	260	2152.2	1.3	1561.5
127	23.2	[18.3, 31.9]	261	[ 196, 306]	19.0	292	260	2160.5	1.3	1575.0
128	23.1	[18.6, 31.5]	253	[ 189, 298]	19.0	285	255	2168.0	1.2	1588.1
129	23.2	[14.1, 37.4]	272	[ 63, 376]	19.6	342	208	2153.7	2.7	1537.4
130	23.8	[14.6, 35.9]	258	[ 67, 362]	20.2	325	117	2143.2	1.7	1554.5

## Data Set S1

Distribution of crustal thickness and output quantities (as shown in Fig. 3) for the reference case (case85 in Tables S1, S2 and S3). Column 1: longitude, Column 2: latitude, Column 3: crustal thickness in km, Column 4: surface heat flow in  $\text{mW/m}^2$ , Column 5: elastic lithosphere thickness (assuming a strain rate of  $10^{-14} \text{ s}^{-1}$ ) in km, Column 6: elastic lithosphere thickness (assuming a strain rate of  $10^{-17} \text{ s}^{-1}$ ) in km, Column 7: temperature in K at 150 km depth, Column 8: depth in km to the 1370 K isotherm, which marks the temperature at the base of the stagnant-lid.

## Data Set S2

Temperature profiles throughout the mantle for the reference case (case85 in Tables S1, S2 and S3). Column 1: radius in km, Column 2: minimum temperature in K attained at each depth, Column 3: average temperature in K at each depth, Column 4: maximum temperature in K attained at each depth, Column 5: temperature in K averaged beneath regions of thin crust (crustal thickness  $\leq$  average crustal thickness), Column 6: temperature in K averaged beneath regions of thick crust (crustal thickness  $>$  average crustal thickness).

## References

- Burov, E.-B., and M. Diament, The effective elastic thickness ( $T_e$ ) of continental lithosphere: What does it really mean?, *J. Geophys. Res.*, *100*, 3905–3927, 1995.
- Filiberto, J., and R. Dasgupta, Constraints on the depth and thermal vigor of melting in the Martian mantle, *Journal of Geophysical Research: Planets*, *120*(1), 109–122, doi:10.1002/2014JE004745, 2015.
- Genova, A., S. Goossens, F. G. Lemoine, E. Mazarico, G. A. Neumann, D. E. Smith, and M. T. Zuber, Seasonal and static gravity field of Mars from MGS, Mars Odyssey and MRO radio science, *Icarus*, *272*(Supplement C), 228 – 245, doi:10.1016/j.icarus.2016.02.050, 2016.
- Grott, M., and D. Breuer, The evolution of the Martian elastic lithosphere and implications for crustal and mantle rheology, *Icarus*, *193*, 503–515, doi:10.1016/j.icarus.2007.08.015, 2008.
- Grott, M., and D. Breuer, On the spatial variability of the Martian elastic lithosphere thickness: Evidence for mantle plumes?, *J. Geophys. Res.*, *115*(E3), doi:10.1029/2009JE003456, 2010.
- Grott, M., D. Baratoux, E. Hauber, V. Sautter, J. Mustard, O. Gasnault, S. W. Ruff, S.-I. Karato, V. Debaille, M. Knapmeyer, F. Sohl, T. V. Hoolst, D. Breuer, A. Morschhauser, and M. J. Toplis, Long-Term Evolution of the Martian Crust-Mantle System, *Space Science Review*, *172*(1), 49–111, doi:10.1007/s11214-012-9948-3., 2013.
- Hahn, B. C., S. M. McLennan, and E. C. Klein, Martian surface heat production and crustal heat flow from Mars Odyssey Gamma-Ray spectrometry, *Geophysical Research Letters*, *38*(14), doi:10.1029/2011GL047435, 2011.

- Hauber, E., P. Brož, F. Jagert, P. Jodłowski, and T. Platz, Very recent and widespread basaltic volcanism on Mars, *Geophysical Research Letters*, *38*(L10201), doi:10.1029/2011GL047310, 2011.
- Hirth, G., and D. Kohlstedt, *Rheology of the Upper Mantle and the Mantle Wedge: A View from the Experimentalists*, pp. 83–105, American Geophysical Union, doi:10.1029/138GM06, 2003.
- Hüttig, C., and K. Stemmer, Finite volume discretization for dynamic viscosities on Voronoi grids, *Physics of the Earth and Planetary Interiors*, *171*(1–4), 137–146, doi:10.1016/j.pepi.2008.07.007, 2008a.
- Hüttig, C., and K. Stemmer, The spiral grid: A new approach to discretize the sphere and its application to mantle convection, *Geochem. Geophys. Geosyst.*, *9*, Q02,018, doi:10.1029/2007GC001581, 2008b.
- Hüttig, C., N. Tosi, and W. B. Moore, An improved formulation of the incompressible Navier-Stokes equations with variable viscosity, *Physics of the Earth and Planetary Interiors*, *40*, 113–129, 2013.
- Jackson, I., U. H. Faul, D. Suetsugu, C. Bina, T. Inoue, and M. Jellinek, Grainsize-sensitive viscoelastic relaxation in olivine: Towards a robust laboratory-based model for seismological application, *Phys. Earth Planet. In.*, *183*, 151–163, doi:10.1016/j.pepi.2010.09.005, 2010.
- Karato, S. I., and P. Wu, Rheology of the upper mantle: a synthesis, *Science*, *260*, 771–778, 1993.
- Keller, T., and P. J. Tackley, Towards self-consistent modeling of the martian dichotomy: The influence of one-ridge convection on crustal thickness distribution, *Icarus*, *202*, 429–443, 2009.
- Kiefer, W. S., J. Filiberto, C. Sandu, and Q. Li, The effects of mantle composition on the peridotite solidus: Implications for the magmatic history of Mars, *Geochimica et Cosmochimica Acta*, *162*, 247–258, 2015.
- Konopliv, A. S., S. W. Asmar, W. M. Folkner, Ö. Karatekin, D. C. Nunes, S. E. Smrekar, C. F. Yoder, and M. T. Zuber, Mars high resolution gravity fields from MRO, Mars seasonal gravity, and other dynamical parameters, *Icarus*, *211*, 401–428, doi:10.1016/j.icarus.2010.10.004, 2011.
- Konopliv, A. S., R. S. Park, and W. M. Folkner, An improved JPL Mars gravity field and orientation from Mars orbiter and lander tracking data, *Icarus*, *274*(Supplement C), 253 – 260, doi:10.1016/j.icarus.2016.02.052, 2016.
- Lainey, V., Quantification of tidal parameters from Solar System data, *Celest. Mech. Dyn. Astr.*, *126*, 145–156, doi:10.1007/s10569-016-9695-y, 2016.
- McNutt, M. K., Lithospheric flexure and thermal anomalies, *Journal of Geophysical Research: Solid Earth*, *89*(B13), 11,180–11,194, doi:10.1029/JB089iB13p11180, 1984.
- Moore, W. B., and G. Schubert, Note: The tidal response of Europa, *Icarus*, *147*, 317–319, doi:10.1006/icar.2000.6460, 2000.

- Neukum, G., R. Jaumann, H. Hoffmann, E. Hauber, J. Head, A. Basilevsky, B. A. Ivanov, S. C. Werner, S. van Gasselt, J. B. Murray, T. McCord, and T. H. C.-I. Team, Recent and episodic volcanic and glacial activity on Mars revealed by the High Resolution Stereo Camera, *Nature*, *432*, 971–979, 2004.
- Newsom, H. E., L. S. Crumpler, R. C. Reedy, M. T. Petersen, G. C. Newsom, L. G. Evans, G. J. Taylor, J. M. Keller, D. M. Janes, W. V. Boynton, K. E. Kerry, and S. Karunatillake, Geochemistry of Martian soil and bedrock in mantled and less mantled terrains with gamma ray data from Mars Odyssey, *J. Geophys. Res.*, *112*(E3), doi:10.1029/2006JE002680, e03S12, 2007.
- Nimmo, F., and U. H. Faul, Dissipation at tidal and seismic frequencies in a melt-free, anhydrous Mars, *J. Geophys. Res.*, *118*(12), 2558–2569, doi:10.1002/2013JE004499, 2013.
- Padovan, S., J.-L. Margot, S. A. Hauck, W. B. Moore, and S. C. Solomon, The tides of Mercury and possible implications for its interior structure, *J. Geophys. Res. Planets*, *119*, 850–866, doi:10.1002/2013JE004459, 2014.
- Phillips, R. J., M. T. Zuber, S. E. Smrekar, M. T. Mellon, J. W. Head, K. L. Tanaka, N. E. Putzig, S. M. Milkovich, B. A. Campbell, J. J. Plaut, A. Safaeinili, R. Seu, D. Biccari, L. M. Carter, G. Picardi, R. Orosei, P. S. Mohit, E. Heggy, R. W. Zurek, A. F. Egan, E. Giacomoni, F. Russo, M. Cutigni, E. Pettinelli, J. W. Holt, C. J. Leuschen, and L. Marinangeli, Mars north polar deposits: Stratigraphy, age, and geodynamical response, *Science*, *320*(5880), 1182–1185, doi:10.1126/science.1157546, 2008.
- Plesa, A. C., N. Tosi, M. Grott, and D. Breuer, Thermal evolution and Urey ratio of Mars, *Journal of Geophysical Research: Planets*, *120*(5), 995–1010, doi:10.1002/2014JE004748, 2015.
- Plesa, A.-C., M. Grott, N. Tosi, D. Breuer, T. Spohn, and M. A. Wieczorek, How large are present-day heat flux variations across the surface of Mars?, *J. Geophys. Res.*, *121*(12), 2386–2403, doi:10.1002/2016JE005126, 2016.
- Ruedas, T., and D. Breuer, On the relative importance of thermal and chemical buoyancy in regular and impact-induced melting in a Mars-like planet, *Journal of Geophysical Research: Planets*, *122*(7), 1554–1579, doi:10.1002/2016JE005221, 2016JE005221, 2017.
- Tosi, N., D. A. Yuen, N. de Koker, and R. M. Wentzcovitch, Mantle dynamics with pressure- and temperature-dependent thermal expansivity and conductivity, *Physics of the Earth and Planetary Interiors*, *217*, 48–58, doi:10.1016/j.pepi.2013.02.004, 2013.
- Van Hoolst, T., V. Dehant, F. Roosbeek, and P. Lognonné, Tidally induced surface displacements, external potential variations, and gravity variations on Mars, *Icarus*, *161*(2), 281 – 296, doi:https://doi.org/10.1016/S0019-1035(02)00045-3, 2003.
- Wänke, H., and G. Dreibus, Chemistry and accretion of Mars, *Philos. Trans. R. Soc. London*, *A349*, 2134–2137, 1994.
- Wieczorek, M. A., Constraints on the composition of the Martian south polar cap from gravity and topography, *Icarus*, *196*(2), 506–517, doi:10.1016/j.icarus.2007.10.026, 2008.

Yoder, C. F., A. S. Konopliv, D. N. Yuan, E. M. Standish, and W. M. Folkner, Fluid Core Size of Mars from Detection of the Solar Tide, *Science*, *300*, 299–303, doi:10.1126/science.1079645, 2003.

Zhao, Y.-H., M. E. Zimmerman, and D. L. Kohlstedt, Effect of iron content on the creep behavior of olivine: 1. Anhydrous conditions, *Earth Planet. Sci. Lett.*, *287*, 229–240, doi:10.1016/j.epsl.2009.08.006, 2009.